

THE EPOCHS OF EARLY-TYPE GALAXY FORMATION AS A FUNCTION OF ENVIRONMENT

DANIEL THOMAS, CLAUDIA MARASTON, RALF BENDER

Max-Planck-Institut für extraterrestrische Physik, Giessenbachstraße, D-85748 Garching, Germany
Universitäts-Sternwarte München, Scheinerstr. 1, D-81679 München, Germany

AND

CLAUDIA MENDES DE OLIVEIRA

Instituto Astronômico e Geofísico, Universidade de São Paulo, Rua do Matão 1226 - Cidade Universitária 05508-900 São Paulo SP -
Brazil

(Received 2004 June, 30; Accepted 2004 October, 5)
The Astrophysical Journal

ABSTRACT

The aim of this paper is to set constraints of the epochs of early-type galaxy formation through the 'archaeology' of the stellar populations in local galaxies. Using our models of absorption line indices that account for variable abundance ratios, we derive ages, total metallicities, and element ratios of 124 early-type galaxies in high and low density environments. The data are analyzed by comparison with mock galaxy samples created through Monte Carlo simulations taking the typical average observational errors into account, in order to eliminate artifacts caused by correlated errors. We find that all three parameters age, metallicity, and α/Fe ratio are correlated with velocity dispersion. We show that these results are robust against recent revisions of the local abundance pattern at high metallicities. To recover the observed scatter we need to assume an intrinsic scatter of about 20 per cent in age, 0.08 dex in $[Z/H]$ and 0.05 dex in $[\alpha/\text{Fe}]$. All low-mass objects with $M_* \lesssim 10^{10} M_\odot$ ($\sigma \lesssim 130$ km/s) show evidence for the presence of intermediate-age stellar populations with low α/Fe ratios. About 20 per cent of the intermediate-mass objects with $10^{10} \lesssim M_*/M_\odot \lesssim 10^{11}$ ($110 \lesssim \sigma/\text{km/s} \lesssim 230$, both ellipticals and lenticulars) must have either a young subpopulation or a blue horizontal branch. Based on the above relationships valid for the bulk of the sample, we show that the Mg- σ relation is mainly driven by metallicity, with similar shares from the α/Fe ratio (23 per cent) and age (17 per cent). We further find evidence for an influence of the environment on the stellar population properties. Massive early-type galaxies in low-density environments appear on average ~ 2 Gyrs younger and slightly ($\sim 0.05 - 0.1$ dex) more metal-rich than their counterparts in high density environments. No offsets in the α/Fe ratios, instead, are detected. With the aid of a simple chemical evolution model, we translate the derived ages and α/Fe ratios into star formation histories. We show that most star formation activity in early-type galaxies is expected to have happened between redshifts ~ 3 and 5 in high density and between redshifts 1 and 2 in low density environments. We conclude that at least 50 per cent of the total stellar mass density must have already formed at $z \sim 1$, in good agreement with observational estimates of the total stellar mass density as a function of redshift. Our results suggest that significant mass growth in the early-type galaxy population below $z \sim 1$ must be restricted to less massive objects, and a significant increase of the stellar mass density between redshifts 1 and 2 should be present caused mainly by the field galaxy population. The results of this paper further imply vigorous star formation episodes in massive objects at $z \sim 2-5$ and the presence of evolved ellipticals around $z \sim 1$, both observationally identified as SCUBA galaxies and EROs, respectively.

Subject headings: galaxies: abundances – galaxies: elliptical and lenticular, cD – galaxies: stellar content – galaxies: formation – galaxies: evolution

1. INTRODUCTION

The most direct way to constrain the formation and evolution of galaxies certainly is to trace back their evolution with redshift (e.g. Aragón-Salamanca et al. 1993; Bender et al. 1996; Kelson et al. 2000; Kodama et al. 1999; Poggianti et al. 1999; Saglia et al. 2000; Stanford et al. 1998; van Dokkum et al. 2000; Ziegler & Bender 1997; Ziegler et al. 1999). The price to be paid, however, is that high-redshift data naturally have lower quality and are therefore more difficult to interpret. A clear complication is the so-called progenitor bias, which implies that galaxies observed at low and high redshift are not necessarily drawn from the same sample (van Dokkum et al. 2000). The alternative approach is the detailed investigation of

the stellar populations in local galaxies, which has been pioneered by analyzing slopes and scatter of color-magnitude and scaling relations of early-type galaxies (e.g. Bender et al. 1992, 1993; Bower et al. 1992; Djorgovski & Davis 1987; Dressler et al. 1987; Renzini & Ciotti 1993), followed by a number of detailed studies of absorption line indices (e.g., Peletier 1989; Gorgas, Efstathiou, & Aragón Salamanca 1990; Worthey, Faber, & González 1992; Davies, Sadler, & Peletier 1993; Carollo & Danziger 1994; Rose et al. 1994; Bender & Paquet 1995; Fisher, Franx, & Illingworth 1995; Jørgensen, Franx, & Kjaergaard 1995; Greggio 1997; Vazdekis et al. 1997; Tantalo, Chiosi, & Bressan 1998; Kuntschner & Davies 1998; Mehlert et al. 1998; Worthey 1998; Kobayashi & Arimoto

1997; Vazdekis & Arimoto 1999; Jørgensen 1999; Terlevich et al. 1999; Kuntschner 2000; Kuntschner et al. 2001; Longhetti et al. 2000; Trager et al. 2000a; Poggianti et al. 2001a,b; Davies et al. 2001; Carter et al. 2002; Proctor & Sansom 2002; Terlevich & Forbes 2002; Saglia et al. 2002; Cenarro et al. 2003; Caldwell, Rose, & Concannon 2003; Mehlert et al. 2003; Thomas, Maraston, & Bender 2003a; and others). We call this the 'archaeology approach'. The confrontation with predictions from models of galaxy formation is certainly most meaningful, when the two approaches, the mining of the high-redshift universe and the archaeology of local galaxies set consistent constraints. In this paper we follow the latter approach.

The main challenge in the archaeology of stellar population is the disentanglement of age and metallicity effects. The use of absorption line indices to lift this degeneracy is powerful (Faber et al. 1985; González 1993; Worthey 1994), but has been up to now hampered by the fact that different metallic line indices yield different metallicities and therefore different ages (see references above). We have solved this problem by developing stellar population models that include element abundance ratio effects and now allow for an un-ambiguous derivation of age, total metallicity, and element ratios from (Lick) absorption line indices (Thomas, Maraston, & Bender 2003b, hereafter TMB). A complication that remains, however, is the degeneracy between age and horizontal branch morphology, which stems from the fact that the presence of warm horizontal branch stars (which cannot be excluded) strengthens the Balmer absorption and can mimic a younger stellar population age (de Freitas Pacheco & Barbuy 1995; Lee et al. 2000; Maraston & Thomas 2000). We will additionally discuss this problem in the present paper.

The principal aim of this study is to constrain the formation epochs of the stellar populations in early-type galaxies as a function of their type (elliptical and lenticular), mass and environmental density. For this purpose we analyze a homogeneous, high-quality data sample of 124 early-type galaxies in various environmental densities. With our new stellar population models (TMB) we determine ages, total metallicities, and α/Fe ratios from the absorption line indices $H\beta$, Mgb , and $\langle\text{Fe}\rangle$, and seek for possible correlations of these parameters with velocity dispersion. First tentative results have already been discussed in Thomas, Maraston, & Bender (2002). Here we present the final and more comprehensive analysis. In particular, we compare the observed data set with mock samples produced through Monte Carlo simulations taking the typical average observational errors into account, in order to eliminate the confusion caused by correlated errors (Kuntschner et al. 2001; Terlevich & Forbes 2002; Trager et al. 2000a).

The α/Fe element ratio plays a key role for the accomplishment of our main goal, namely the derivation of formation epochs. While the so-called α -elements O, Ne, Mg, Si, S, Ar, Ca, Ti (particles that are build up with α -particle nuclei) plus the elements N and Na are delivered mainly by Type II supernova explosions of massive progenitor stars, a substantial fraction of the Fe-peak elements Fe and Cr comes from the delayed exploding Type Ia supernovae (e.g. Nomoto, Thielemann, & Yokoi

1984; Thielemann, Nomoto, & Hashimoto 1996; Woosley & Weaver 1995). Hence, the α/Fe ratio quantifies the relative importance of Type II and Type Ia supernovae (Greggio & Renzini 1983; Matteucci & Greggio 1986; Pagel & Tautvaisiene 1995; Thomas, Greggio, & Bender 1998), and therefore carries information about the timescale over which star formation occurs. Thus, the α/Fe ratio can be considered as an additional measure of late star formation, and we will use it both to constrain formation timescales and to lift the degeneracy between age and horizontal branch morphology.

The paper is organized as follows. In Sections 2 and 3 we present the methodology of the paper, i.e. we introduce the data sample, we briefly summarize the stellar population model of TMB, and we explain the construction of the mock galaxy sample through Monte Carlo simulations. The results of this analysis are presented in Section 4. We use these results to explore the origin of the $\text{Mg}-\sigma$ relation (Section 5) and to derive star formation histories (Section 6) with the aim to constrain the epoch of early-type galaxy formation. The main results of the paper are discussed and summarized in Sections 7 and 8.

2. THE DATA SAMPLE

2.1. Sample selection

We analyze a sample of 124 early-type galaxies, 70 of which reside in low-density and 54 in high-density environments, containing roughly equal fractions of elliptical and lenticular (S0) galaxies. To maintain statistical significance, in the following we make the rough bimodal distinction between low-density and high-density environment. It should be emphasized that the classification 'low density' comprises galaxies in environments with low density, not necessarily isolated objects. The sample is constructed from the following sources: 41 galaxies in high (Virgo cluster) and low density environments (González 1993), 32 Coma cluster galaxies (Mehlert et al. 2000, 2003), and 51 galaxies (mostly low density environment) from Beuing et al. (2002) selected from the ESO-LV catalog (Lauberts & Valentijn 1989) (highest-quality objects). In this latter sample, objects with a local galaxy surface density $\text{NG}_T > 9$ are assigned to the high density environment. NG_T is given in Lauberts & Valentijn (1989) and is the number of galaxies per square degree inside a radius of one degree around the considered galaxy (see Beuing et al. 2002). The sample spans a large range in central velocity dispersion $60 \lesssim \sigma_0/\text{kms}^{-1} \lesssim 340$ with similar distributions in both environments (Fig. 1).

In the data samples quoted above, absorption line strengths are measured as functions of galaxy radius. We adopt the central indices determined within 1/10 of the effective radius, so that the analysis presented here does not suffer from aperture effects. We use the Lick indices $H\beta$, Mgb , and $\langle\text{Fe}\rangle = 0.5(\text{Fe}5270 + \text{Fe}5335)$ to derive the stellar population parameters age t , total metallicity $[Z/H]$, and the element abundance ratio $[\alpha/\text{Fe}]$. The medians of the 1- σ errors in $H\beta$, Mgb , $\text{Fe}5270$, and $\text{Fe}5335$ are 0.06, 0.06, 0.07, 0.08 Å, respectively.

We have re-observed 19 objects of the Beuing et al. (2002) sample with the same telescope (the 1.5m tele-

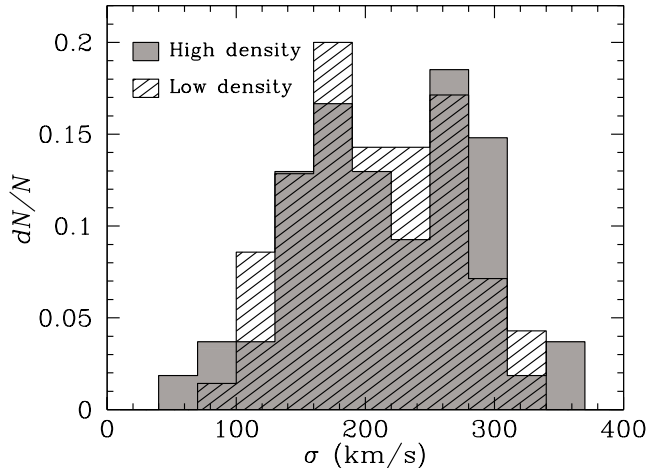


FIG. 1.— Distribution of central velocity dispersion in high density (grey shaded histogram) and low density (hatched histogram) environments.

scope on La Silla) with the principal aim of extending the wavelength range to the blue (Mendes de Oliveira et al., in preparation). We find a good agreement for the optical absorption line indices $H\beta$, Mgb , and $\langle Fe \rangle$ between the two samples, with a small systematic offset in Mgb of 0.2 \AA . As the latter observations have higher quality due to the installation of a new CCD chip and holographic grating, we corrected for the offset in Mgb and replaced the values of Beuing et al. (2002) with the new measurements for the objects in common. We emphasize here, however, that the results of this paper are not affected by this procedure.

2.2. Absorption line indices

In Fig. 2 we present the absorption line index measurements plotting $[MgFe]'$ vs. $H\beta$ (top panels) and Mgb vs. $\langle Fe \rangle$ (bottom panels). The index

$$[MgFe]' = \sqrt{Mgb \cdot (0.72 \cdot Fe5270 + 0.28 \cdot Fe5335)},$$

a slight modification of $[MgFe]$ defined by González (1993), is almost completely independent of α/Fe ratio variations (TMB). Left and right panels show data in high density and low density environments, respectively. Red symbols are elliptical, blue symbols are lenticular, and green symbols are cD galaxies. Overplotted are our stellar population models (TMB) for various ages, metallicities, and α/Fe ratios as indicated by the labels in the diagrams.

2.2.1. TMB models

The TMB models take the effects from element abundance ratio changes on all Lick indices into account, hence give Lick indices of simple stellar populations (SSPs) not only as functions of age and metallicity but also as a function of the α/Fe ratio. They are based on the evolutionary population synthesis code of Maraston (1998, 2005). In Thomas et al. (2003b), the impact from element ratio changes is computed with the help of the Tripicco & Bell (1995) response functions, using an extension of the method introduced by Trager et al. (2000b). The updated version used in this paper adopts the new metallicity-dependent response

functions from Korn, Maraston, & Thomas (2005). As discussed there, the impact of metallicity on the response functions for the indices considered here is negligible (see also Thomas, Maraston, & Korn 2004), hence does not affect the results of this paper.

Particular care was taken to calibrate the SSP models with globular cluster data (Maraston et al. 2003), which—most importantly—include objects with relatively high, namely solar, metallicities (Puzia et al. 2002). We match very well their $H\beta$, Mgb , and $\langle Fe \rangle$ indices with models in which the α/Fe ratio is enhanced by a factor two relative to the solar value, in agreement with results from high-resolution spectroscopy of individual stars (see TMB and Maraston et al. 2003, and references therein). Because of the inclusion of element ratio effects, the models allow for the clear distinction between total metallicity $[Z/H]$ and the α to iron-peak elements ratio $[\alpha/Fe]$.

We use these models to derive the three stellar population parameters age, metallicity, and α/Fe ratio from the three line indices $H\beta$, Mgb , and $\langle Fe \rangle$ in a twofold iterative procedure explained below. As mentioned in the Introduction, there is a degeneracy between age and horizontal branch morphology. A way to lift this degeneracy is the consideration of the α/Fe ratio. We expect young stellar populations generally to be characterized by lower α/Fe ratios owing to the late enrichment of Fe from Type Ia supernovae.

In this paper we present a detailed investigation of the data set based on Monte Carlo simulations as shall be discussed in the following sections. However, first tentative conclusions can already be drawn by the direct comparison between the observational data and SSP model grids, as discussed in the following.

2.2.2. Ages and metallicities

The index $[MgFe]'$ is a good tracer of total metallicity (still degenerate with age, of course), as it is almost completely independent of α/Fe ratio variations (TMB). As also $H\beta$ is only very little sensitive to α/Fe (TMB), the top panels of Fig. 2 are well suited to read off ages and total metallicities independent of abundance ratio effects.

The sample splits in two subclasses divided by the Balmer absorption index at $H\beta \approx 2 \text{ \AA}$. The main part of the data is centered around $H\beta = 1.6 \text{ \AA}$, while about one quarter of the objects have relatively high $H\beta$ absorption implying the presence of either young stellar populations or blue horizontal branch morphologies (Maraston & Thomas 2000). This surprisingly well-defined separation is also discussed in Mehlert et al. (2003) for the Coma cluster objects alone. Interestingly, the pattern is still present for the larger galaxy sample considered here, and in particular the fraction of high $H\beta$ objects seems to be independent of the environmental density (Fig. 2), but we do not find a significant difference with respect to the galaxy type. Fig. 2 further hints toward a difference between objects as a function of environment within the old (low $H\beta$) class, in the sense that galaxies in low density environments seem to have on average slightly younger ages and higher metallicities. This difference is more clearly visible in the direct comparison of the derived ages discussed below.

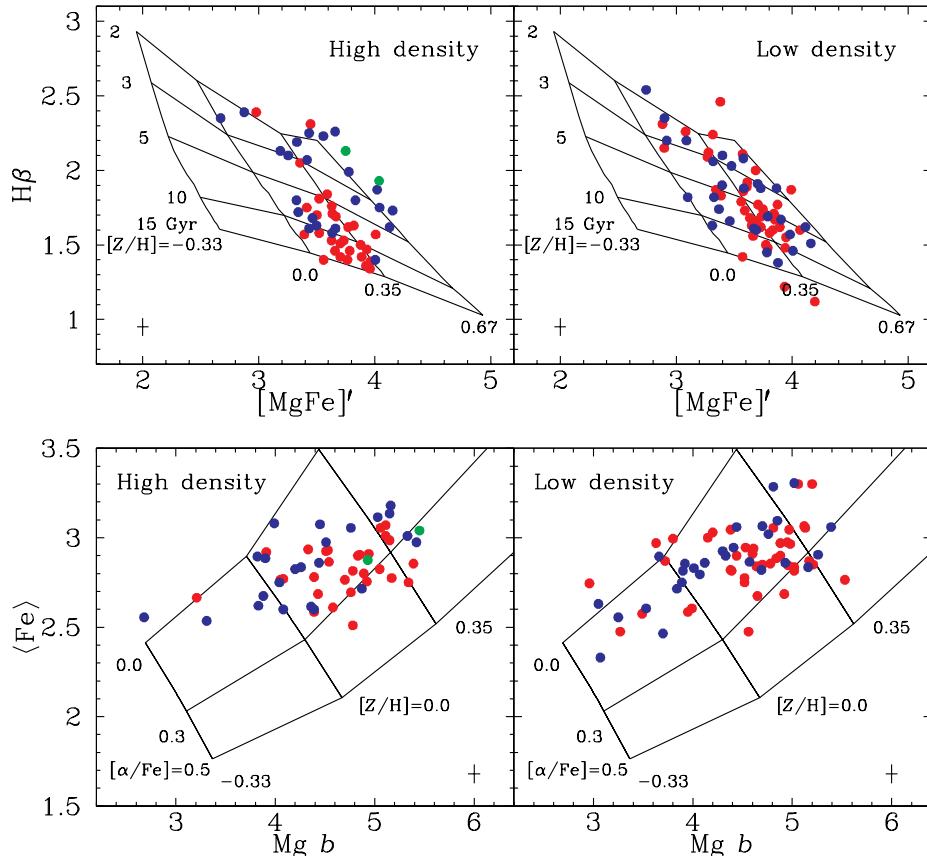


FIG. 2.— Lick indices $[MgFe]'$ versus $H\beta$ (top panels) and $Mg\ b$ versus $\langle Fe \rangle$ (bottom panels). Symbols are the early-type galaxies analyzed in this paper, taken from González (1993), Beuing et al. (2002), and Mehler et al. (2003). Index values are measured within $\sim 1/10\ r_e$. Left and right panels show objects in high and low density environments, respectively. Red symbols are elliptical, blue symbols lenticular, and green symbols are cD galaxies. Median $1-\sigma$ error bars are shown. SSP models (TMB) with the metallicities $[Z/H] = 0.0, 0.35, 0.67$ with the metallicity $[Z/H] = 0.0$ (top panels) and different α/Fe ratios $[\alpha/Fe] = 0.0, 0.3, 0.5$ at fixed age ($t = 12$ Gyr) (bottom panels) as indicated by the labels.

2.2.3. Element abundance ratios

The bottom panel of Fig. 2 can be used to get rough estimates for the α/Fe ratios of the sample galaxies. It should be emphasized, however, that the $Mg\ b$ - $\langle Fe \rangle$ plane is not completely degenerate in age, and the ages derived from the top panels have to be taken into account for the precise derivation of α/Fe ratios. Still we can infer from the bottom panels of Fig. 2 that the α/Fe ratios range roughly between solar and two times solar, and that objects with strong $Mg\ b$ indices, hence velocity dispersion because of the Mg - σ relation (e.g. Bender et al. 1993), tend to have higher α/Fe ratios. At least no obvious impact from environmental density on the α/Fe ratios is visible.

2.2.4. Derivation of stellar parameters

The stellar population parameters are derived in a two-fold iterative procedure. First, we arbitrarily fix the α/Fe ratio, and determine ages and metallicities for the index pairs $(H\beta, Mg\ b)$ and $(H\beta, \langle Fe \rangle)$, by starting with arbitrary age-metallicity pairs, which we modify iteratively until both index pairs are reproduced. The two metallicities obtained from $Mg\ b$ and $\langle Fe \rangle$, respectively, are used to adjust the α/Fe ratio, and to start a new iteration. These steps are repeated until the age-metallicity pairs

derived from $(H\beta, Mg\ b)$ and $(H\beta, \langle Fe \rangle)$ at a given α/Fe ratio are consistent within 1 per cent accuracy. For ages and metallicities between the grid points quoted above, we interpolate linearly.

The resulting ages, metallicities, and α/Fe for the sample under investigation are listed in Table A3.

3. THE MONTE CARLO APPROACH

An uncomfortable effect of the degeneracy between age and metallicity is that the errors of these stellar population parameters are not independent. It is still a matter of debate, for instance, whether the age-metallicity anti-correlation found for early-type galaxies in a number of studies is an artifact caused by correlated errors (Jørgensen 1999; Kuntschner et al. 2001; Poggianti et al. 2001b; Proctor & Sansom 2002; Terlevich & Forbes 2002; Trager et al. 2000a). A possibility to get a handle on these effects is the performance of Monte Carlo simulations taking into account the observational uncertainties of the line indices from which the stellar population parameters are derived. Kuntschner et al. (2001) follow this method in order to assess the relationship between ages and metallicities of 72 early-type galaxies by comparison with a mock sample produced through Monte Carlo simulations.

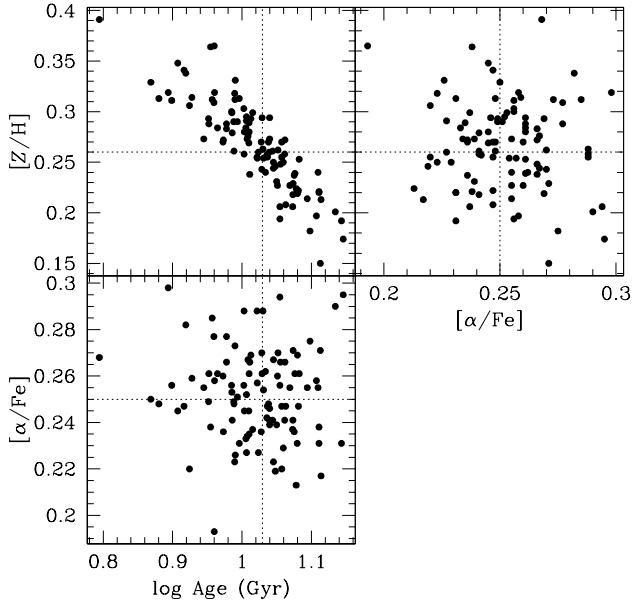


FIG. 3.— Stellar population parameters of an object with $H\beta = 1.59 \text{ \AA}$, $Mgb = 4.73 \text{ \AA}$, and $\langle Fe \rangle = 2.84 \text{ \AA}$ corresponding to an age of 10.7 Gyr, a metallicity $[Z/H] = 0.26$, and $[\alpha/Fe] = 0.25$ as indicated by the dotted lines. The circles are Monte Carlo realizations perturbing the original index values with the $1-\sigma$ errors $dH\beta = 0.06 \text{ \AA}$, $dMgb = 0.06 \text{ \AA}$, $dFe5270 = 0.07 \text{ \AA}$, and $dFe5335 = 0.08 \text{ \AA}$. The resulting $1-\sigma$ errors of the stellar population parameters are 1.48 Gyr in age, 0.04 dex in total metallicity, and 0.02 dex in α/Fe ratio.

In this paper we extend the approach of Kuntschner et al. (2001) to the full parameter space including also α/Fe ratios besides age and total metallicity. We produce a sample of artificial galaxies with given ages, metallicities, and α/Fe ratios, from which we compute with the TMB SSP models the line indices $H\beta$, Mgb , and $\langle Fe \rangle$. By means of Monte Carlo simulations we perturb these ‘exact’ values with the $1-\sigma$ errors quoted above, assuming a Gaussian error distribution. An illustrative example for the resulting correlations between the errors of the three population parameters is given in Fig. 3 for an artificial object with $H\beta = 1.59 \text{ \AA}$, $Mgb = 4.73 \text{ \AA}$, and $\langle Fe \rangle = 2.84 \text{ \AA}$ corresponding to an age of 10.7 Gyr, a metallicity $[Z/H] = 0.26$, and $[\alpha/Fe] = 0.25$ indicated by the dotted lines. The circles are 100 Monte Carlo realizations taking the $1-\sigma$ errors in the line indices ($dH\beta = 0.06 \text{ \AA}$, $dMgb = 0.06 \text{ \AA}$, $dFe5270 = 0.07 \text{ \AA}$, $dFe5335 = 0.08 \text{ \AA}$) into account.

The distributions of the resulting stellar population parameters can be well described by Gaussians. The corresponding $1-\sigma$ errors are 1.48 Gyr in age, 0.04 dex in total metallicity, and 0.02 dex in α/Fe ratio. We confirm that errors produce a very tight linear anti-correlation between log age and metallicity (top left panel) as already mentioned above. Interestingly, we find that also the errors of age and α/Fe ratio are anti-correlated (bottom left panel). This relationship is the result of the slightly stronger age dependence of the Mgb index with respect to $\langle Fe \rangle$, caused by the larger contribution from turnoff stars to Mgb and Mg_2 (Maraston et al. 2003). An underestimation of the age leads to the prediction

of lower Mg indices relative to iron, which results in the derivation of a larger α/Fe ratio, and vice versa.

In the following Monte Carlo simulations will be used to reproduce and analyze the distribution of the data in the diagrams shown in Fig. 2. The simulations are carried out in two steps, low density and high density environments are considered separately throughout the analysis.

1) First, we seek correlations between galaxy velocity dispersion and the stellar population properties age, metallicity, and α/Fe ratio that reproduce the majority of the data sample. Indeed, Trager et al. (2000a) have already shown that velocity dispersion is the only structural parameter that is found to modulate the stellar populations of galaxies. As we aim at deriving average properties, simple stellar populations of single age and single chemical composition are used. We start with the velocity dispersion (σ) distribution of the data sample shown in Fig. 1. Based on arbitrarily chosen relationships, we assign to every σ an age, metallicity, and α/Fe ratio, which we transform into $H\beta$, Mgb , and $\langle Fe \rangle$. These indices are then perturbed with the observational error (see above) adopting a Gaussian probability distribution. In this way we obtain a mock galaxy sample that is closest to the observational situation in terms of size, velocity dispersion distribution, and error perturbation. If necessary, we add an intrinsic scatter in the stellar population parameters age, metallicity, and α/Fe . This step is repeated, until the majority of the observed data points in the index-index diagrams $[MgFe]'$ vs. $H\beta$ and Mgb vs. $\langle Fe \rangle$ is reproduced (comparison ‘by eye’). The quality of the fit is further checked with respect to the zero points, slopes, and scatter of the relationships between the stellar parameters (age, metallicity, α/Fe ratio) and velocity dispersion. By means of the index-index diagrams we identify those objects that are not reproduced by the mock data sample based on the simple relationships introduced in this step.

2) In a second step, we therefore perturb the general simple scaling laws found in the first step in 2-component models in order to match those remaining objects. Like before, we adopt the exact σ distribution of the outliers and assign age, metallicity and α/Fe to every σ based on the above final relationships to define the base population. Then we add a second component with arbitrary stellar population parameters and determine the index values of this composite population. These are then perturbed like in the first step and compared to the observational data. We note that the contribution in mass of the second component is treated as the fourth free parameter, hence the solutions will not be unique, as we have only three observables as constraints ($H\beta$, Mgb , $\langle Fe \rangle$). As discussed in detail below, we will use plausibility arguments trying to maintain astrophysical feasibility of the Monte Carlo realizations, in order to constrain the relative weights of the subcomponents.

4. RESULTS

In Fig. 4 the comparison of our Monte Carlo realizations (black symbols) with the observational data (colored symbols) is shown in the index-index planes introduced with Fig. 2. By means of the ‘age-metallicity’ diagram (top panels of Fig. 4) we distinguish between four different categories, independent of the environment, as

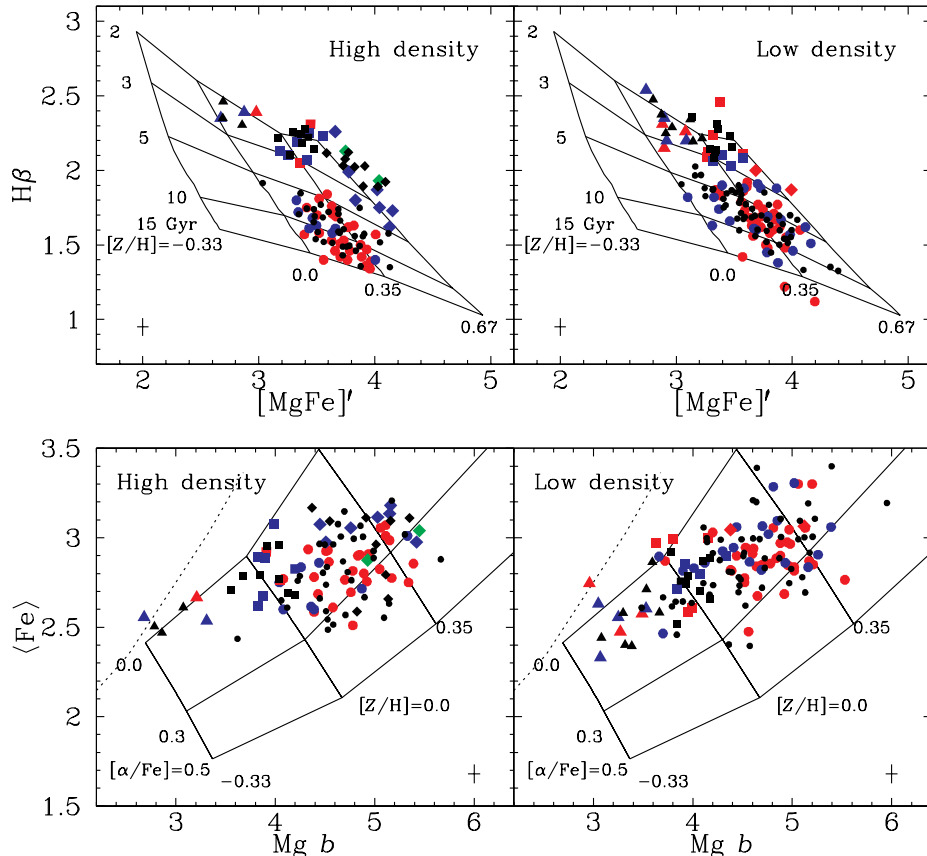


FIG. 4.— Lick indices $[\text{MgFe}]'$ versus $H\beta$ (top panels) and $\text{Mg } b$ versus $\langle \text{Fe} \rangle$ (bottom panels). Colored symbols are the early-type galaxies analyzed in this paper (red: elliptical, blue: S0, green: cD), taken from González (1993), Beuing et al. (2002), and Mehlert et al. (2003), measured within $1/10 r_e$. Median $1-\sigma$ error bars are shown. Black symbols are Monte Carlo realizations. Circles assume linear relationships of age, metallicity and α/Fe ratio with velocity dispersion (see Eqn. 1). Triangles and squares are simulations assuming 1.2 and 1.4 Gyr old subcomponents (10 and 20 per cent in mass, respectively) on top of the above relationships, respectively. Diamonds are realizations in which 70 per cent of the galaxy's stellar populations is assumed to form around a look back time of 2.5 Gyr (see Tables 1 and A2). Left and right panels show objects in high and low density environments, respectively. SSP models (TMB) with the metallicities $[Z/\text{H}] = 0.0, 0.35, 0.67$ are plotted for different ages $t = 2, 3, 5, 10, 15$ Gyr at fixed α/Fe ratio ($[\alpha/\text{Fe}] = 0$) (top panels) and different α/Fe ratios $[\alpha/\text{Fe}] = 0.0, 0.3, 0.5$ at fixed age ($t = 12$ Gyr) (bottom panels) as indicated by the labels. Dotted lines in the bottom panels are models for $t = 2$ Gyr and $[\alpha/\text{Fe}] = 0$.

indicated by the symbol types: 1) V -light averaged ages older than ~ 5 Gyr (circles), 2) ages between 2 and 3 Gyr and metallicities $[Z/\text{H}] \lesssim 0.35$ (triangles), 3) ages between 2 and 3 Gyr and metallicities $0.35 \lesssim [Z/\text{H}] \lesssim 0.67$ (squares), 4) ages between 2 and 5 Gyr and metallicities $[Z/\text{H}] \gtrsim 0.67$ (diamonds).

Here we provide a short summary how these categories are reproduced, detailed descriptions are discussed below in Sections 4.1 to 4.4. Category 1 contains intermediate-mass and massive galaxies ($120 \lesssim \sigma/(\text{km/s}) \lesssim 320$) and can be reproduced by linear relationships between the stellar population parameters and $\log \sigma$. For simplicity we shall call this category *old population*, as Categories 2–4, unlike Category 1, require 2-component models with young sub-populations. Category 2 consists of *low-mass galaxies* ($50 \lesssim \sigma/(\text{km/s}) \lesssim 130$) and are reproduced assuming a minor (10 per cent in mass) young (~ 1.2 Gyr) sub-component. Category 3 are *young intermediate-mass galaxies* ($110 \lesssim \sigma/(\text{km/s}) \lesssim 230$) with a minor (20 per cent in mass) young (~ 1.4 Gyr) component, while Category 4 contains *young massive galaxies* ($190 \lesssim \sigma/(\text{km/s}) \lesssim 360$) with a major (70 per

TABLE 1. MODEL PARAMETERS

	circles	triangles	squares	diamonds
σ (km/s)	120–320	50–130	110–230	190–360
$\log M_*/M_\odot$	10–12	< 10	10–11	> 11
1st comp.	Eqn. 1	Eqn. 1	Eqn. 1	Eqn. 1
2nd comp.	no	yes	yes	yes
Mass	–	10%	20%	70%
Age (Gyr)	–	1.2	1.4	2.5
$[Z/\text{H}]$	–	~ 0.2	~ 0.8	~ 0.7
$[\alpha/\text{Fe}]$	–	~ -0.06	~ 0.20	~ 0.34

Note. — Stellar masses (row 2) are from Eqn. 2. The last five rows refer to the second component.

cent in mass) young (~ 2.5 Gyr) component. The data sample is well characterized by these four object classes and well reproduced by the Monte Carlo simulations. In the following section we will discuss in detail their characteristics. They are summarized in Table 1 and A2.

4.1. Old population - circles

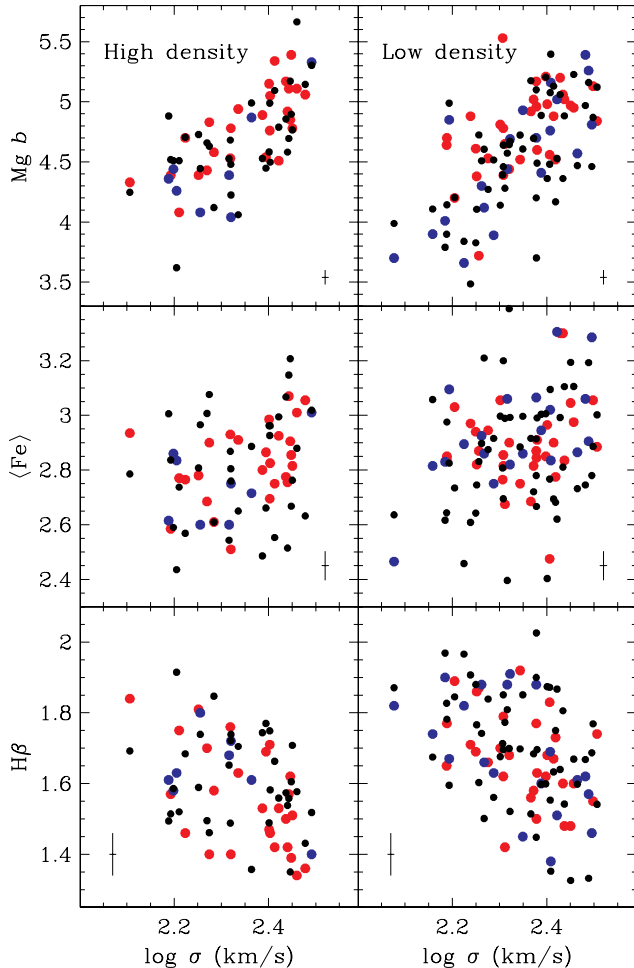


FIG. 5.— Absorption line indices as a functions of velocity dispersion (measured within $1/10 r_e$) for the ‘old’ subpopulation shown as circles in Fig. 4 (red: elliptical, blue: S0, green: cD, taken from González (1993), Beuing et al. (2002), and Mehlert et al. (2003), measured within $1/10 r_e$). Median $1-\sigma$ error bars are shown. The Monte Carlo realizations are shown by the black symbols. The latter take the observational errors (see Fig. 3) into account plus an intrinsic scatter $\Delta[\alpha/\text{Fe}] = 0.05$ dex, $\Delta[Z/\text{H}] = 0.08$ dex, and $\Delta t = 0.2 \cdot t$ Gyr in high density environments (left panel) and $\Delta[\alpha/\text{Fe}] = 0.07$ dex, $\Delta[Z/\text{H}] = 0.10$ dex, and $\Delta t = 0.25 \cdot t$ Gyr in low-density environments (right panel).

This subpopulation represents the major fraction of the present sample, namely 60 and 70 per cent in high density and low density environments, respectively containing both elliptical and lenticular galaxies. The objects display relatively well-defined relationships between absorption line indices and central velocity dispersion, as shown in Fig. 5 by the colored symbols. Both metallic indices $\text{Mg } b$ and $\langle \text{Fe} \rangle$ correlate with velocity dispersion, which is well-known for $\text{Mg } b$ (e.g., Bender et al. 1993), and has also been recently established for $\langle \text{Fe} \rangle$ (Bernardi et al. 2003; Caldwell et al. 2003; Kuntschner et al. 2001). The Balmer index $\text{H}\beta$, instead, clearly tends to decrease with increasing σ (see also Bernardi et al. 2003; Caldwell et al. 2003; Kuntschner et al. 2001). Fig. 5 shows that these relationships are essentially independent of the environment, except that the $\langle \text{Fe} \rangle$ - σ relation seems somewhat flatter in low-density environments.

4.1.1. Scaling relations

The black symbols in Fig. 5 are the Monte Carlo realizations corresponding to the dominating ‘old’ population (circles in Fig. 4). In these simulations we have assumed linear correlations of the parameters age, metallicity and α/Fe ratio with $\log \sigma$. The dependencies that fit best all three indices as functions of velocity dispersion for objects in high density environments are (quantities in brackets are the values derived for the low-density environment):

$$[\alpha/\text{Fe}] = -0.42 (-0.42) + 0.28 (0.28) \log \sigma \quad (1)$$

$$[Z/\text{H}] = -1.06 (-1.03) + 0.55 (0.57) \log \sigma$$

$$\log t/\text{Gyr} = 0.46 (0.17) + 0.238 (0.32) \log \sigma$$

The simulations take the observational errors (see Fig. 3) into account plus an intrinsic scatter $\Delta[\alpha/\text{Fe}] = 0.05$ dex, $\Delta[Z/\text{H}] = 0.08$ dex, and $\Delta t = 0.2 \cdot t$ Gyr in high density environments and $\Delta[\alpha/\text{Fe}] = 0.07$ dex, $\Delta[Z/\text{H}] = 0.10$ dex, and $\Delta t = 0.25 \cdot t$ Gyr in low-density environments. The relationships with velocity dispersion including their scatter of the line indices are well reproduced. The relative contributions of the observational errors and the intrinsic scatter of the stellar population parameters to the overall spread in the data and simulations will be discussed in more detail below.

Before doing so, we provide estimates of the stellar masses as a function of velocity dispersion. For this purpose we transform the ages and metallicities of Eqn. 1 into stellar mass-to-light ratios with the help of stellar population models and use these to derive (via the Faber-Jackson relation, Faber & Jackson 1976) a relationship between stellar mass and velocity dispersion. We adopt the SSP models of Maraston (2005) for Kroupa IMF (note that a Salpeter IMF yields M/L ratios, hence masses, by a factor 1.6 higher). The M/L ratios (and masses) derived in this way from the high density and low density relationships vary by only 25 per cent, because the younger ages of the low density objects are balanced by higher metallicities. In the following equation we therefore provide the resulting relationship between stellar mass M_* and $\log \sigma$ averaged over both environments.

$$\log M_* \approx 0.63 + 4.52 \log \sigma \quad (2)$$

This yields the following relations between the stellar population parameters and galaxy stellar mass.

$$[\alpha/\text{Fe}] = -0.459 (-0.459) + 0.062 (0.062) \log M_*/M_\odot(3)$$

$$[Z/\text{H}] = -1.137 (-1.109) + 0.1217 (0.1261) \log M_*/M_\odot$$

$$\log t/\text{Gyr} = 0.427 (0.125) + 0.053 (0.071) \log M_*/M_\odot$$

4.1.2. Stellar population parameters

Fig. 6 shows velocity dispersion and stellar mass versus the stellar population parameters age, metallicity $[Z/\text{H}]$, and $[\alpha/\text{Fe}]$ ratio derived from the line indices shown in Fig. 5. They are summarized in Table A3. Observational data are the colored symbols (see Fig. 2), the Monte Carlo realizations are shown as black circles. The lines indicate the linear relationships of the stellar population parameters with $\log \sigma$ used in the simulations (see Eqn. 1). The residuals of the data and Monte Carlo simulations from these relationships are shown in Fig. 7 by

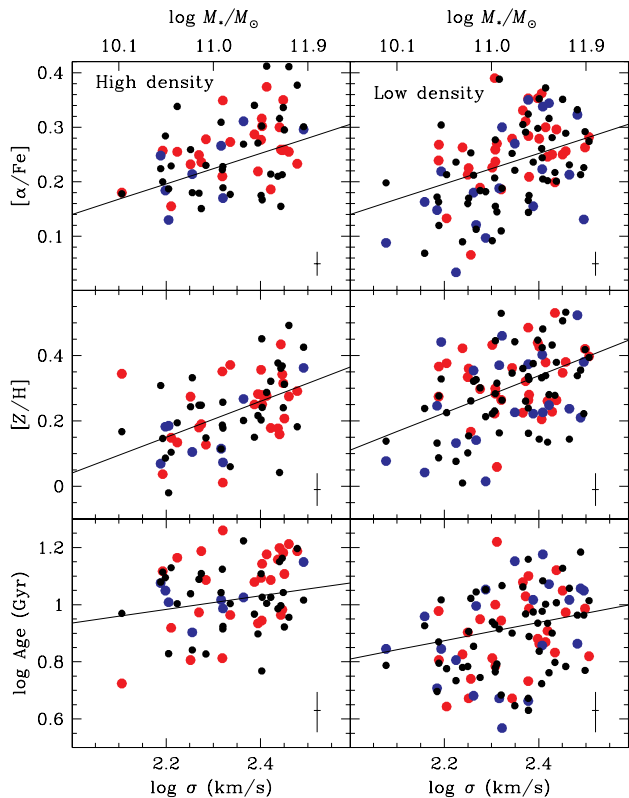


FIG. 6.— Stellar population parameters as a functions of velocity dispersion (measured within $1/10 r_e$) and stellar mass (upper x-axis) for the ‘old’ subpopulation (circles in Fig. 4 and Fig. 5). Ages and element abundances are derived with the $[\alpha/\text{Fe}]$ enhanced SSP models described in Section 2 from the indices $H\beta$, $\text{Mg } b$, and $\langle \text{Fe} \rangle = (\text{Fe}5270 + \text{Fe}5335)/2$. Colored symbols are the values derived from the observational data (red: elliptical, blue: S0, green: cD), median $1-\sigma$ error bars are shown. The Monte Carlo realizations are shown by the black circles. The latter take the observational errors (see Fig. 3) into account plus an intrinsic scatter $\Delta[\alpha/\text{Fe}] = 0.05$ dex, $\Delta[Z/\text{H}] = 0.08$ dex, and $\Delta t = 0.2 \cdot t$ Gyr in high density environments (left panel) and $\Delta[\alpha/\text{Fe}] = 0.07$ dex, $\Delta[Z/\text{H}] = 0.10$ dex, and $\Delta t = 0.25 \cdot t$ Gyr in low-density environments (right panel). Typical error-bars are given in the bottom-right corners.

the grey and hatched histograms, respectively. Note that the simulations take both the observational errors plus an intrinsic scatter of the stellar population parameters at a given σ ($\Delta[\alpha/\text{Fe}] = 0.05$ dex, $\Delta[Z/\text{H}] = 0.08$ dex, and $\Delta t = 0.2 \cdot t$ Gyr in high density environments and $\Delta[\alpha/\text{Fe}] = 0.07$ dex, $\Delta[Z/\text{H}] = 0.10$ dex, and $\Delta t = 0.25 \cdot t$ Gyr in low-density environments) into account. The red histograms are simulations without intrinsic scatter for comparison.

α/Fe We find a very clear correlation between α/Fe ratio and $\log \sigma$ or stellar mass. The existence of this relation has already been anticipated qualitatively by a number of authors (e.g. Fisher et al. 1995; Greggio 1997; Jørgensen 1999; Kuntschner 2000; Terlevich & Forbes 2002; Worthey et al. 1992), and has only recently been confirmed quantitatively by means of stellar population models with variable element abundance ratios (Mehlert et al. 2003; Proctor & Sansom 2002; Thomas et al. 2002; Trager et al. 2000a). The observed scatter about the relation can only be reproduced assuming an intrinsic scatter in $[\alpha/\text{Fe}]$ ratio of the order

0.05 dex as shown by the hatched histograms in Fig. 7. In the simulations without intrinsic scatter (red histograms in Fig. 7), the scatter in α/Fe is significantly smaller than the observed distribution.

Most interestingly, as already shown in Thomas et al. (2002), the $\alpha/\text{Fe}-\sigma$ relation (and its scatter) of early-type galaxies is independent of the environmental density (see also Eqn. 1). This reinforces and extends the results of the studies by Jørgensen, Franx, & Kjørgaard (1995) and Terlevich & Forbes (2002), which are based on stellar population models tied to solar element ratios. Curiously, early-type galaxies in low density environments seem to exhibit stronger CN absorption features than in high density environments (Sanchez-Blazquez et al. 2003). As a significant fraction of C and N comes from intermediate-mass stars in the mass range $5 \lesssim M/M_\odot \lesssim 8$ (Renzini & Voli 1981), this points toward about 10^8 years longer formation timescales in low density environments. A delay well above this value can certainly be excluded, as the α/Fe ratio is independent of the environment. Hence, if true the above result means that there must be an amazingly high degree of fine tuning in the formation timescales of early-type galaxies as a function of environmental density.

Z/H Besides α/Fe , also total metallicity Z/H correlates with σ , hence more massive early-type galaxies are also more metal-rich (see also Greggio 1997). This result is sensible in terms of chemical evolution, as the deeper potential well of massive objects hampers the development of a galactic wind, which leads to a more complete chemical processing to higher element abundances (e.g. Arimoto & Yoshii 1987; Edmunds 1990; Matteucci 1994). The observational scatter is best reproduced assuming about 0.1 dex of intrinsic scatter in total metallicity at a given velocity dispersion (hatched histograms in Fig. 7). Different from the α/Fe ratio, however, simulations without intrinsic scatter still provide a reasonable representation of the data (red histograms in Fig. 7).

Unlike for the α/Fe ratio, we detect a slight impact of the environmental density in the sense that galaxies in low density environments appear about 0.05–0.1 dex more metal-rich than their counterparts in high density environments (see also Eqn. 1). This implies that galaxies in high-density environments seem to be more efficient in ejecting interstellar material in galactic winds, which might be caused by galaxy interactions and/or gas stripping processes.

Age As noted in previous studies (Kuntschner et al. 2001; Terlevich & Forbes 2002; Trager et al. 2000a), age seems to be the weakest variable among early-type galaxies, the data show no significant trend between age and velocity dispersion. However, it has also been shown by Kuntschner et al. (2001) that correlated errors of age and metallicity tend to dilute a correlation between age and metallicity, because a slight overestimation of Z/H leads to an underestimation of the age and vice versa. In Fig. 6 we show that the observational data are best reproduced by a relatively flat but significant correlation between age and velocity dispersion (see solid lines and Eqn. 1) in agreement with previous studies (Proctor, Forbes, & Beasley 2004; Proctor et al. 2004; Proctor & Sansom 2002). The scatter of the observationally derived age (and of the Balmer index $H\beta$, see

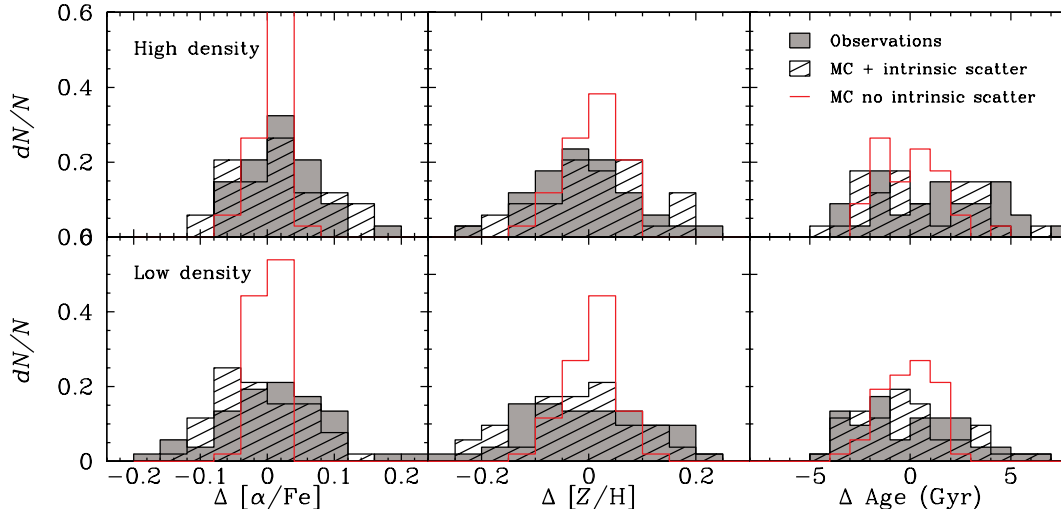


FIG. 7.— Residuals of the relations shown in Fig. 6 for the observationally derived data (grey histograms) and the simulations (hatched histograms). The latter take the observational errors (see Fig. 3) plus an intrinsic scatter $\Delta[\alpha/\text{Fe}] = 0.05$ dex, $\Delta[Z/\text{H}] = 0.08$ dex, and $\Delta t = 0.2 \cdot t$ Gyr in high density environments (top panels) and $\Delta[\alpha/\text{Fe}] = 0.07$ dex, $\Delta[Z/\text{H}] = 0.10$ dex, and $\Delta t = 0.25 \cdot t$ Gyr in low-density environments (bottom panels) into account. The red histograms show the residuals of simulations without intrinsic scatter of the stellar population parameters.

Fig. 5) is relatively well reproduced by the simulations without any intrinsic scatter (red histograms in Fig. 7). A scatter of the order of 20 per cent at a given σ improves the fit as shown by the hatched histograms in Fig. 7.

To conclude, the mean age of early-type galaxies is weakly correlated with galaxy mass with about 20 per cent intrinsic scatter. From this anti-hierarchical relationship we infer that the stellar populations of more massive early-type galaxies have formed earlier, which is further supported by their high α/Fe ratios.

Unlike in the case of the α/Fe ratio and total metallicity, we find a significant difference between the ages of galaxies in high- and low-density environments. There is a clear offset indicating that the stellar populations of early-type galaxies in low density environments are on average about 2 Gyr younger in agreement with previous results (Caldwell et al. 2003; Kuntschner et al. 2002; Poggianti et al. 2001b; Proctor et al. 2004; Terlevich & Forbes 2002; Trager et al. 2000a). This relative age difference caused by environmental effects is in very good agreement with the predictions from semi-analytic models of galaxy formation (Kauffmann & Charlot 1998).

4.2. Low-mass galaxies - triangles

The objects of the low-mass tail of the velocity dispersion distribution (Fig. 1) with stellar masses $M_* < 10^{10} M_\odot$ (Eqn. 2) exhibit all relatively high Balmer indices, indicating light-averaged ages between 2 and 3 Gyr (triangles in Fig. 4). We recover these objects with 2-component composite stellar population models based on the ‘old population’ (circles in Fig. 4) the properties of which are specified in Eqn. 1. Extrapolation to the appropriate σ yields ages between 6 and 8 Gyr for the base old population. The average ages of the low-mass objects in both environments are then matched by contaminating this base old population with a 10 per cent contribution (in mass) of a young (~ 1.2 Gyr) population (see filled

triangles in Fig. 4). As mentioned earlier, this is certainly not a unique solution, as the contribution in mass and the look-back time of the star formation event are highly degenerate and therefore only poorly constrained. Alternatively, also the addition of a major young component contributing 70 per cent in mass with an age of 2 Gyr reproduces the observed line indices. We can conclude, however, that relatively recent star formation in low-mass early-type galaxies is required to explain the observational data (see also Trager et al. 2000a).

The model with the minor young component gets some support from the α/Fe ratios. The bottom panel of Fig. 4 shows that also the Mg- and Fe- indices are well reproduced by assuming that the young component is 0.2 dex less α/Fe enhanced than the base old population. This clearly favors the option of a young component over the possible presence of old blue horizontal branch stars as an explanation for the relatively strong Balmer absorption observed in low-mass galaxies. The metal indices of the objects are relatively weak, we needed to assume the young component to be about 0.2 dex more metal-rich than the base old population.

4.3. Young intermediate-mass galaxies - squares

This subpopulation of objects with velocity dispersions between 110 and 230 km/s, hence $7 \cdot 10^9 \lesssim M_*/M_\odot \lesssim 2 \cdot 10^{11}$ (see Eqn. 2), represents a minor fraction of the whole sample, namely ~ 14 per cent containing both elliptical and lenticular types. There is no obvious dependence on environmental density and galaxy type. We consider the slight bias toward more lenticulars in high-density environments (6 S0s out of 8 early-types in high density vs. 4 S0s out of 9 early-types in low density) as statistically not significant given the relatively small sample size.

The striking feature of these objects is their relatively strong Balmer line index, yielding light-average ages between 2 and 4 Gyr. To reproduce their $\text{H}\beta$ indices, we

model these galaxies with a 2-component model adding a minor young component as described in the previous paragraph. Different from low-mass galaxies, however, are the metallicities of the young subcomponent. To match the relatively strong $[\text{MgFe}]'$ index observed, extraordinarily high metallicities for the young component are required. The smaller the contribution (in mass) of the subcomponent is, the higher its metallicity needs to be. The avoidance of unplausibly high metallicities ($[Z/H] \gtrsim 0.8$ dex) sets therefore a lower limit to the weight of the subpopulation. Metallicities below that limit are ensured, if the young subpopulation contributes at least 20 per cent in mass. For this lower limit, an age of 1.4 Gyr and metallicities around $[Z/H] \sim 0.8$ dex are required to reproduce the observational data. An upper limit can not be constrained. The high metallicity of the young component points toward a much higher effective yield during the formation of the young component in these intermediate-mass objects, compared to the low-mass objects discussed above. This means that chemical evolution and the build-up of metals is less efficient in low-mass objects, in agreement with the general picture that objects with shallower potential wells develop galactic winds easier (e.g. Arimoto & Yoshii 1987; Chiosi & Carraro 2002; Edmunds 1990; Matteucci 1994).

Also different from the case of the low-mass galaxies, we had to assume the young population to have the same α/Fe ratio like the base old population, in order to reproduce their Mg- and Fe-indices (bottom panel of Fig. 4, compare to dotted model lines for $t = 2$ Gyr). This spoils the interpretation of the enhanced Balmer line strengths in terms of the presence of an intermediate-age stellar population. The separation in age between the old and young components amounts to several billion years, plenty of time for Type Ia supernovae to enrich the interstellar medium with iron. Forming out of this Fe-enhanced material, it will be impossible for the young component to reach significantly super-solar α/Fe ratios. Even the self-enrichment of the young component from Type II supernovae during the burst is not sufficient to raise the average α/Fe ratio of the newly born stellar populations independent of the burst timescale as shown in Thomas et al. (1999).

The interpretation of the observed strong Balmer line indices in terms of recent star formation could be recovered under the rather contrived assumption that the Type Ia supernova ejecta originating from stars of the base old population have been lost selectively in galactic winds before the formation of the young subpopulation. Alternatively, the latter must have formed with a stellar initial mass function (IMF) significantly flatter than Salpeter. A flat IMF slope would naturally reproduce the very high metallicity of the young component derived here. On the other hand, compelling evidences for systematic variations of the IMF slope in starbursts have not been found so far (Leitherer 1998).

But we have to be cautious here. Relatively high α/Fe ratios are needed for the young subpopulation, because in the models $\text{Mg } b$ decreases significantly with decreasing age at highest metallicity, and it is possible that the fitting functions are in error in this regime owing to bad input stellar data. On top of this, the extraordinarily high metallicities of the young subcomponent ($[Z/H] \sim 0.8$) require extrapolation well above the highest metallicity

model ($[Z/H] = 0.67$), which makes the model indices very unreliable. The relatively low $\text{Mg } b$ index of the model, which causes the need for the relatively high α/Fe ratio, might be an artifact of bad calibration. To conclude, lower values for the young subpopulation cannot be excluded, which rehabilitates the possibility of the presence of an intermediate-age population.

Alternatively, the strong Balmer lines might be the result of blue horizontal branch stars rather than a young population, which we shall discuss in detail below.

4.4. *Young massive galaxies - diamonds*

Finally, the diamonds indicate a subclass of very massive early-type galaxies ($M_* > 10^{11} M_\odot$) that have strong $\text{H}\beta$ and strong $[\text{MgFe}]'$ absorption indices, implying light-averaged ages between 2 and 5 Gyr, and very high metallicities of $[Z/H] \gtrsim 0.67$ dex. From Fig. 4 it can be seen that the occurrence of these objects is restricted to high-density environments. Moreover, they are only lenticular galaxies, no ellipticals with such low average ages and high metallicities are found (see Fig. 4). The vast majority (80 per cent) of all S0 galaxies with $\sigma > 200$ km/s in our sample and the two Coma cD galaxies belong to this object class (see also Kuntschner 2000; Mehlert et al. 2003; Poggianti et al. 2001b).

The metallicities are more than 0.2 dex above the average metallicity of the most massive objects in the old base population constrained by Eqn. 1. Such a significant increase in average metallicity can obviously not be obtained in a 2-component model with only 10–20 per cent of a metal-rich subpopulation, unless unreasonable high metallicities above ten times solar are assumed. We therefore have to increase the weight of the young population. The filled diamonds shown in Fig. 4 are models in which the old base population is 'perturbed' with a 2.5 Gyr young population with metallicities as high as $[Z/H] \sim 0.7$ dex contributing 70 per cent in mass. Lower metallicities can be adopted only under the assumption that an even larger fraction of the stellar populations belongs to the second component.

Interestingly, like in the previous case these objects have very high α/Fe ratios. For the young component we need to adopt α/Fe ratios as they are given by Eqn. 1, hence $[\alpha/\text{Fe}] > 0.2$ for $\sigma > 200$ km/s. This fits well into the picture that the young average ages are not the result of minor recent star formation, but rather the consequence of a recent very massive star formation event at a redshift around $z = 0.3$ forming the majority of the galaxy's stellar populations on a short timescale. This would imply that massive S0s and cD galaxies in clusters form very recently, while ellipticals of comparable mass contain only old stellar populations. This explanation seems contrived, and it remains to be seen if it can be understood in the framework of galaxy formation models.

4.5. *Blue horizontal branch stars at high metallicities*

Alternatively, the strong $\text{H}\beta$ indices discussed above might be caused by the presence of metal-rich, blue horizontal branch stars (see Introduction). Such blue horizontal branch stars may originate from either a metal-poor subpopulation as discussed in Maraston & Thomas (2000) or metal-rich populations with blue horizontal branch morphologies due to enhanced mass loss along

the red giant branch evolutionary phase. Here we consider this latter option.

4.5.1. *The origin of blue horizontal branches*

The mass-loss along the red giant branch can be theoretically understood as stellar winds being produced by the acoustic flux generated by the superadiabatic convection in the outer convective zone of the red giant (Fusi-Pecci & Renzini 1975). The fraction of acoustic energy which is used to remove the stellar envelope is not known from physically motivated, first principles. An alternative is the empirical determination of the mass loss rate, which has been done by Reimers (1975) studying the behavior of the circumstellar calcium K line in a large number of red giants and supergiants. The normalization of the resulting formula, however, suffers from very large uncertainties.

Fusi-Pecci & Renzini (1976) combined the two approaches and introduced an efficiency factor η for Reimer's formula. They calibrated the mass loss rate with observational constraints like the horizontal branch morphology (Rood 1973), the limiting initial mass for carbon ignition ($\sim 4 M_{\odot}$ for the Hyades van den Heuvel 1975), and finally the solar mass loss rate. An efficiency $\eta \approx 0.33$ turned out to be the most appropriate choice. This value is adopted in the models of Maraston (1998, 2005). Note that the observational uncertainties in Reimer's formula allow this efficiency factor to lie in the range $0.3 \lesssim \eta \lesssim 3$. The problem is that the calibration has been carried out at sub-solar metallicity, and deviations from this canonical value, in particular at higher metallicities, cannot be excluded (Greggio & Renzini 1990).

4.5.2. *Effect on the line indices*

The models of TMB are based on Maraston (1998, 2005), thus rely on the calibrated value $\eta = 0.33$. Here we additionally compute models with the slightly larger efficiency factor $\eta = 0.55$, which is well within the range of uncertainty allowed by the Reimer's formula. These models have bluer horizontal branch morphologies, and therefore predict significantly stronger Balmer indices, and slightly weaker metallic indices. This is shown in the left panel of Fig. 8 by the arrow labeled 'HB' for a 10 Gyr old population. The arrow labeled 'age' shows the location of a model with age $t = 1.5$ Gyr, which yields the same $H\beta$ value, for comparison. The steeper slope of the 'HB' model illustrates the weaker sensitivity of the metallic line indices to HB morphology than to age. The relative effect of $Mg\ b$ and $\langle Fe \rangle$ is shown in the right panel of Fig. 8. Relative to $\langle Fe \rangle$ the $Mg\ b$ index responds stronger to a decrease of age than to a blueing of the horizontal branch. As a consequence, the slope of the 'HB' model is steeper also in the $Mg\ b$ - $\langle Fe \rangle$ diagram. Note that the slope is comparable to the model varying metallicity at a constant α/Fe ratio and age.

4.5.3. *2-component model*

These results will mainly affect the age determination. To test this, we have constructed a 2-component model in which the base old population is contaminated with 50 per cent of an old metal-rich population with blue horizontal branch stars. The location of both the squares and

the diamonds in Fig. 4 is reached by these models, hence without invoking the presence of intermediate-age populations. We had to assume the metallicity of the second component to be about 0.2–0.4 dex higher than the average of the base population, while the α/Fe ratio needs to be about 0.1 dex lower. Hence, the blue HB option requires the assumption that preferentially the metal-rich stars in a composite stellar population develop blue horizontal branches. The slightly lower α/Fe ratios would fit into this picture, as the most metal-rich populations must have formed latest and should therefore be least α/Fe enhanced.

4.5.4. *Young vs. blue horizontal branch*

To conclude, none of the two options—intermediate-age population or blue horizontal branch—can be excluded, further observational constraints to distinguish the two alternative explanations are required.

If intermediate-age populations are present in these galaxies, they should be detectable by their very red near-infrared colors, because of the major contribution to the bolometric from asymptotic giant branch stars at ages between 0.5 and 2 Gyr (Maraston 1998, 2004, 2005; Maraston et al. 2001).

Un-ambiguous indicators of blue horizontal branches, instead, still need to be found. The CaII index defined by Rose (1984), even though promising, does not solve the problem as it is still degenerate between gravity and metallicity effects. Schiavon et al. (2004) show that in metal-poor globular clusters the higher-order Balmer line index $H\delta_F$ is more sensitive to the presence of blue horizontal branches than $H\beta$. Hence, the index ratio $H\delta_F/H\beta$ may be a tool to break the degeneracy between age and horizontal branch morphology. It is not clear, however, if this effect is still present at solar metallicities and above, which are relevant to massive galaxies. Moreover, in Thomas et al. (2004) we show that at such high metallicities the $H\delta_F/H\beta$ index ratio becomes very sensitive to the α/Fe ratio in the sense that $H\delta_F/H\beta$ increases with α/Fe . If blue horizontal branches ought to be detected in early-type galaxies by means of the $H\delta_F/H\beta$ ratio, the dependence on α/Fe certainly has to be taken into account. It will be interesting to make these checks for the galaxy sample discussed here. Such an analysis will be subject of a future study.

5. THE ORIGIN OF THE Mg - σ RELATION

The correlations of the stellar population parameters age, total metallicity, and α/Fe ratio with central velocity dispersion shown in Fig. 6 and Eqn. 1 allow us to constrain the origin of the well-known Mg - σ relation (top panels of Fig. 5). We recall that the correlations found here suggest that all three parameters correlate with σ , hence support the Mg - σ relationship.

Fig. 9 shows the observed $Mg\ b$ - σ relation of the whole sample high density and low density environments combined. It can be verified from Fig. 5 that the environment has a negligible effect on the Mg - σ relation in agreement with previous findings based on much larger samples (Bernardi et al. 1998; Colless et al. 1999; Worthey & Collobert 2003). Circles are the 'old population' representing the major fraction of the sample, triangles, squares, and diamonds are the 'young outliers' discussed in the previous section (see also Fig. 4). Red

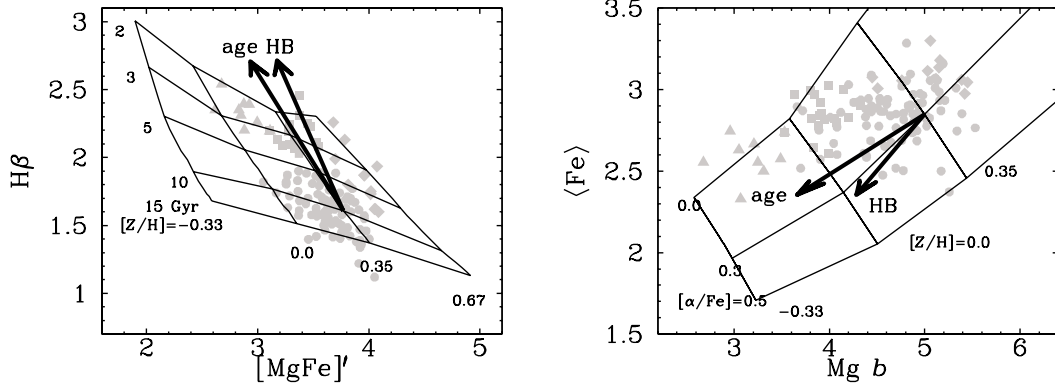


FIG. 8.— Comparison of the effects of age and blue horizontal branch on the absorption indices $H\beta$, $Mg b$, and $\langle Fe \rangle$. Symbols and model grid like in Fig. 4. The arrows labeled ‘HB’ show the index changes of a 10 Gyr population ($[Z/H] = 0.35$, $[\alpha/Fe] = 0.3$, RGB mass loss parameter $\eta = 0.33$) when a blue horizontal branch $\eta = 0.55$ is considered. For comparison, the effect of reducing the age to 1.5 Gyr is indicated by the arrows labeled ‘age’.

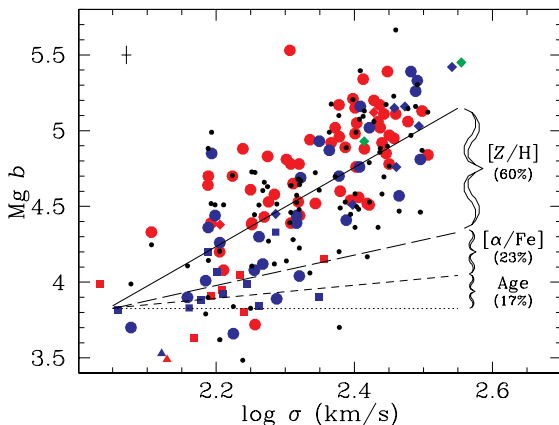


FIG. 9.— $Mg b$ - σ relation of the whole sample high density and low density environments combined. Colored symbols are observational data (red: elliptical, blue: S0, green: cD), median $1-\sigma$ error bars are shown. Black symbols Monte Carlo simulations (symbol types like in Fig. 4). The solid line is the $Mg b$ - σ relation resulting from the relationships given in Eqn. 1 averaging over high and low density environments. The short-dashed line shows the resulting $Mg b$ - σ relation if only age is assumed to be the driving parameter adopting Eqn. 1. The long-dashed line demonstrates the effect of additionally adding the dependence on α/Fe ratio from Eqn. 1.

and blue symbols are elliptical and lenticular galaxies. Green symbols are cD galaxies. The black symbols are the Monte Carlo realizations. The solid line is the $Mg b$ - σ relation that results from the relationships given in Eqn. 1 (averaging over both environments). The short-dashed line shows the resulting $Mg b$ - σ relation if only age is assumed to be the driving parameter adopting Eqn. 1. The dependencies of both total metallicity and α/Fe ratio with σ are suppressed. The long-dashed line demonstrates the effect of additionally adding the dependence on α/Fe ratio from Eqn. 1.

It can be seen that total metallicity has by far the largest share (60 per cent) in shaping the relation, followed by the α/Fe ratio contributing only 23 per cent to the observed slope. The contribution from age is about 17 per cent, hence is smallest but comparable to the one

of α/Fe . We emphasize that these numbers do not vary significantly with environmental density. As can be inferred from Figs. 5 and 6, the scatter of the $Mg b$ - σ relation among the old population (circles) results from intrinsic scatter in all three stellar population parameters. The $\langle Fe \rangle$ - σ relation is much shallower (see Fig. 5) because the increasing α/Fe ratio with σ diminishes the $\langle Fe \rangle$ -index, compensating largely the increase due to increasing metallicity (see also Mehlert et al. 2003).

This result fits very well to the fact that also the color-magnitude relation appears to be driven by metallicity rather than age (Kodama & Arimoto 1997; Merluzzi et al. 2003; Stanford et al. 1998; Terlevich et al. 1999; Vazdekis et al. 2001), even though the effect of the α/Fe ratio variations on colors is still not very well understood (Thomas & Maraston 2003).

Finally, we briefly examine the location of the ‘young outliers’ of Fig. 4 (triangles, squares and diamonds). The low-mass and intermediate-mass objects with young light-averaged ages (triangles and squares) are clearly off the relation and exhibit systematically lower index values (by $\sim 0.5 \text{ \AA}$) at a given σ . Their slightly larger light-averaged metallicities (see Fig. 4) do obviously not suffice to bring them back on the relationship. Different the class of massive, apparently young Coma cluster lenticulars (diamonds). Their extremely high light-averaged metallicities compensate totally for the decrease in $Mg b$ caused by the young light-averaged ages. As far as the $Mg b$ - σ relation is concerned, these objects are indistinguishable from the main body of the sample.

6. FORMATION EPOCHS

The relations shown in Fig. 6 (see also Eqns. 1 and 3) can be used to constrain the epochs of the main star formation episodes and the star formation timescales for early-type galaxies as a function of their mass and environmental densities. It should be emphasized that the majority of the objects of the present sample obeys these relationships. Only 15 per cent of the sample (squares in Fig. 4) requires a 20 per cent contribution from intermediate age populations on top of the base old population described by Eqn. 1, and further 9 per cent (diamonds)

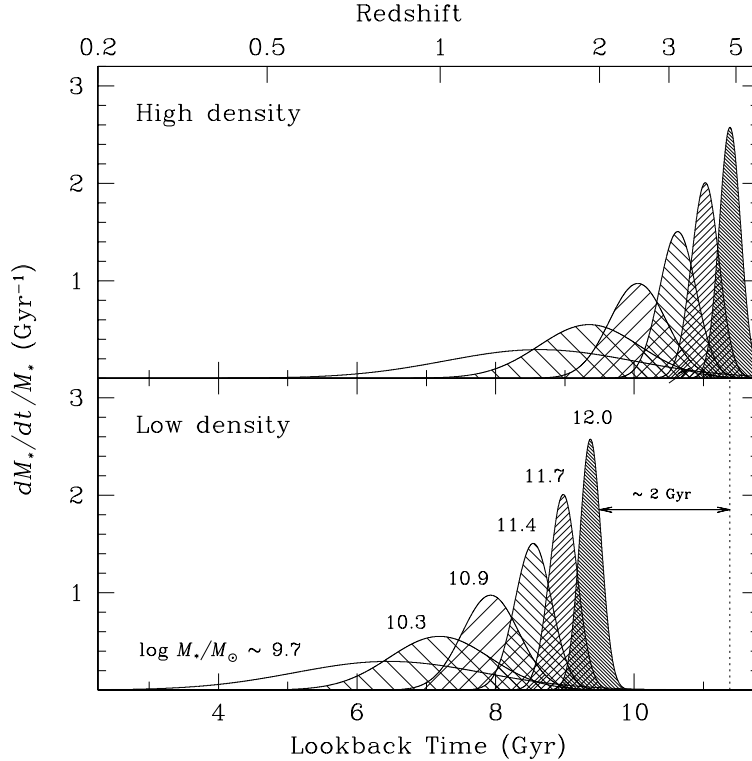


FIG. 10.— Star formation histories of early-type galaxies as a function of their stellar masses M_* (see labels). The stellar masses M_* correspond to the velocity dispersions $\sigma = 100, 140, 190, 240, 280, 320$ km/s (see Eqn 2). The star formation histories are derived from the mean ages and $[\alpha/\text{Fe}]$ ratios shown in Fig. 6 and Eqns. 1 (or 3) and 4. Redshifts assume $\Omega_m = 0.3$, $\Omega_\Lambda = 0.7$, $H_0 = 75$ km/s/Mpc (Spergel et al. 2003). The dotted lines marks the average age of a high density objects with $M_* = 10^{11} M_\odot$ ($\sigma = 320$ km/s) for comparison.

are best modeled assuming 70 per cent young populations. The young low-mass galaxies (triangles in Fig. 4) do not play a significant role in the total mass budget of early-type galaxies, the latter being dominated by L^* galaxies with $M_* \sim 10^{11} M_\odot$ situated at the turnover of the luminosity (mass) function (Baldry et al. 2004; Bell et al. 2003). This implies that about 90 per cent of the total stellar mass hosted by early-type galaxies is well represented by the relationships given in Eqn. 1.

6.1. Relating timescale and α/Fe ratio

The key point of this analysis is that the α/Fe ratio lifts the degeneracy between formation epoch and formation timescale. This is done by relating the observationally derived luminosity-averaged α/Fe ratios of the stellar populations with timescales of their formation.

For this purpose we simulate the formation and chemical evolution of a set of toy galaxies assuming various star formation histories characterized by different timescales similar to the exercise presented in Thomas et al. (1999).

We start with a gas cloud of primordial chemical composition. By imposing a star formation rate as a function of time, which is given by the specific star formation history assumed, we let the gas cloud form stars. These stars enrich the gas of the cloud (the interstellar medium) with heavy elements produced mainly in supernova explosions. For the aim of this paper we follow the chemical enrichment of α and Fe-peak elements. A key point is that we take the delayed enrichment of Fe from

Type Ia supernovae into account using the prescription of Greggio & Renzini (1983, see Thomas et al. 1998 for more details). Stellar populations successively form out of more and more chemically enriched gas, resulting in the build-up of a composite stellar population. Every generation of stars in this composite will have the chemical composition, hence α/Fe ratio, of the gas out of which it had formed. We examine this population 12 Gyr after the formation of the first stellar generation, and calculate its V -light averaged $[\alpha/\text{Fe}]$ ratio, which corresponds to the quantity observationally derived in this study. The weight in V -luminosity of the single stellar populations as a function of their ages is adopted from the M/L ratios of Maraston (2004). The IMF slope is kept fixed to Salpeter. Like in Thomas et al. (1999), the simulations are carried out assuming a closed box, which implies that selective mass-loss is assumed not to occur and thus not to affect the α/Fe ratio.

The star formation histories in the different runs are chosen to be Gaussians of various widths Δt (FWHM). We find the following linear relationship between α/Fe ratio and $\log \Delta t$:

$$[\alpha/\text{Fe}] \approx 1/5 - 1/6 \log \Delta t. \quad (4)$$

The equation reflects what has already been shown in Thomas et al. (1999), namely that a ratio $[\alpha/\text{Fe}] = 0.2$ of a composite stellar population requires formation timescales $\Delta t \lesssim 1$ Gyr. The larger Δt , the lower is the final α/Fe ratio of the stellar population because of

the late enrichment of Fe from Type Ia supernovae. Star formation extended over the Hubble time yields an α/Fe close to solar. We note that this link between α/Fe ratio and star formation timescale is in very good agreement with the more detailed chemical evolution simulations of Pipino & Matteucci (2004).

The combination of Eqns. 1 and 3 with Eqn. 4 then yields correlations of Δt with σ and mass for early-type galaxies valid in both high and low environmental densities.

$$\begin{aligned} \log \Delta t &\approx 3.44 - 1.68 \log \sigma \\ &\approx 3.67 - 0.37 \log M_*/M_\odot \end{aligned} \quad (5)$$

Eqns. 1 and 3 further give the light-average ages as a function of σ , constraining the epoch at which the object has formed.

6.2. The star formation histories

The resulting star formation histories for various galaxy masses and velocity dispersions are shown in Fig. 10. The x-axis is lookback time, the upper x-axis gives the corresponding redshifts assuming $\Omega_m = 0.3$, $\Omega_\Lambda = 0.7$, and $H_0 = 75 \text{ km/s/Mpc}$ (Spergel et al. 2003). The top and bottom panels show the results for dense and loose environments, respectively.

It should be kept in mind that Fig. 10 is based on average ages and α/Fe ratios at a given mass. As discussed in Section 4, the data require a scatter in α/Fe ratio of the order 0.05 – 0.07 dex (see Fig. 7), which translates into a spread in star formation timescale of about a factor 2. The observed spread in average age is consistent with the a scatter of about 20–25 per cent (see Fig. 7). For a cluster early-type galaxy with stellar mass $M_* \sim 5 \cdot 10^{11} M_\odot$ ($\sigma = 280 \text{ km/s}$), for instance, this implies a spread about the typical formation redshift at $z \sim 3$ between $z \sim 2$ and $z \sim 5$. The blurring caused by these effects should be kept in mind for the interpretation of the diagrams in Fig. 10, which are meant to be a schematic illustrations of the mean formation epochs.

6.3. Dependence on galaxy mass

The plots summarize what has been already discussed in the previous sections. The more massive the galaxy is, the faster and earlier form its stellar populations. Indeed Pipino & Matteucci (2004) show that the observed relation between α/Fe and σ can be best reproduced by a model in which gas accretion and star formation timescales decrease with increasing galaxy mass. Only low-mass galaxies exhibit significant star formation at redshifts below $z \lesssim 1$ as also concluded by Brinchmann & Ellis (2000) and more recently De Lucia et al. (2004). These results are also in very good agreement with the star formation histories found by Gavazzi et al. (2002) based on spectrophotometric data. Interestingly, the link between star formation histories and galaxy mass shown in Fig. 10 agrees well with the predictions from N-body-tree-SPH simulations by Chiosi & Carraro (2002), which are based on a monolithic collapse inside a dark matter halo rather than hierarchical structure formation.

Note that we have assumed continuous star formation in order to keep the number of free parameters low. The principal aim of this exercise is to illustrate the typical timescale of the star formation histories in galaxies

as a function of their masses. In reality, star formation in individual objects will be less smooth and will be shaped by several bursty star formation episodes (see Chiosi & Carraro 2002). The functions of Fig. 10 thus have to be understood as integrals at a given velocity dispersion over bursty star formation histories. In particular the extended star formation histories of the low-mass objects might rather be understood in terms of episodically returning star forming bursts, similar to what is found in dwarf galaxies of the Local Group (Mateo 1998).

In massive systems, the burst might well be triggered by merger events. Indeed, a considerable fraction of massive ellipticals have kinematically decoupled cores (Bender 1988; Franx & Illingworth 1988), the presence of which requires the merger to be accompanied by dissipational processes and star formation. Interestingly, for a number of ellipticals with kinematically decoupled cores, it has been found that their stellar populations are homogeneously old and α/Fe enhanced (Davies et al. 2001; Mehlert et al. 1998; Surma & Bender 1995), indicating the merger to have happened at early times, in agreement with the formation histories of Fig. 10 (a counterexample is NGC 2865, Hau, Carter, & Balcells 1999).

6.4. Influence of the environment

The second main result is that galaxy formation appears delayed by $\sim 2 \text{ Gyr}$ in low density environments confirming previous findings (Caldwell et al. 2003; Kuntschner et al. 2002; Poggianti et al. 2001b; Proctor et al. 2004; Terlevich & Forbes 2002; Trager et al. 2000a).

This is in agreement with studies of the field galaxy population at intermediate redshifts around $z \sim 1$ (Gebhardt et al. 2003; Treu et al. 2002; van Dokkum et al. 2001). While the formation of massive early-type galaxies in clusters sets in at redshifts around $z \sim 5$ and is completed (in terms of their stellar populations) at about $z \sim 2$, a considerable fraction of massive galaxy formation in low density environments occurs at lower redshifts between $z \sim 1$ and $z \sim 2$. We recall here that the α/Fe - σ relation does not depend on environmental density. The timescale of star formation in an object is determined by its (final) mass rather than the environment. As a consequence, massive early-type galaxies in low density environments form later but on similar timescales like their counterparts in high environmental densities as illustrated in Fig. 10.

7. DISCUSSION

7.1. The local abundance pattern at high metallicities

In a recent study, Proctor et al. (2004) argue that the correlation of α/Fe with velocity dispersion is an 'artefact of incomplete calibration (of the models) to the Lick system'. The basis for their conclusion is the recent finding of Bensby et al. (2004), that the Milky Way disk stars with super-solar metallicities do not have solar but sub-solar O/Fe ratios, O/Fe decreasing with increasing Fe/H (see also Allende Prieto et al. 2004; Pompéia et al. 2003). Stellar population models, being calibrated with these stars, are then likely to reflect sub-solar O/Fe ratios at high metallicities. If the element Oxygen is taken as representative for all α -elements, this would obviously lead to an overestimation of the O/Fe ratio (or α/Fe ratio) in stellar populations with super-solar metallicities

like early-type galaxies. Proctor et al. (2004) show that the correction for this effect makes the $\alpha/\text{Fe}-\sigma$ relation disappear.

However, there is a further very important (and somewhat puzzling) point shown in Bensby et al. (2004). All the other α -elements, Mg, Si, Al, Na, Ca, and Ti, do not show this pattern, but level-off at a solar X/Fe ratio in stars with super-solar metallicities (Bensby et al. 2003; Fuhrmann 1998). Only the element oxygen (and maybe also carbon, Thorén, Edvardsson, & Gustafsson 2004) sticks out of this homogeneous behavior. This differential pattern between Oxygen and the other α -elements cannot be neglected in models taking the local abundance pattern at high metallicities into account. This is particularly important in the context of this work, as the α/Fe ratios presented here are derived from the absorption line indices $\text{Mg } b$ and $\langle \text{Fe} \rangle$, which are sensitive mostly to the elements Fe and Mg, but *not* O (Korn et al. 2005; Tripicco & Bell 1995).

We investigated this issue constructing two additional flavors of stellar population models that account for this local abundance pattern at high metallicities. The first model takes oxygen as representative for all α -elements (like in Proctor et al. 2004), in the second model oxygen is detached from the rest of the α -elements as discussed above. The resulting models in the index-index planes and the stellar population parameters derived with these models are shown in Figs. B11 and B13 (equivalent to Fig. 2) and Figs. B12 and B14 (equivalent to Fig. 2) in the Appendix. The results are discussed in detail there.

To summarize, we reproduce the result of Proctor et al. (2004) with the model in which oxygen and α -element are not separated. The $\alpha/\text{Fe}-\sigma$ relation disappears, the $Z/\text{H}-\sigma$ relation becomes tighter, while the ages remain unchanged. When oxygen is detached from the other α -elements as suggested by observations, the picture is entirely different as explained in detail in Section B. The correction for the local abundance pattern has no significant impact on the model, when the non-solar O/Mg ratios of metal-rich stars in the solar neighborhood are taken into account. The model basically moves back to its original position. As a consequence, the stellar population parameters derived with this model are in excellent agreement with the ones presented in this work (see Fig. B14).

To conclude, the results of this paper are robust against the correction for the local abundance pattern at high metallicities. In particular, the $\alpha/\text{Fe}-\sigma$ relation found here is real and is not caused by calibration artefacts. What remains to be understood is the discrepancy between oxygen and the other α -elements in the metal-rich stars of the solar neighborhood.

As discussed in Bensby et al. (2004), a possible explanation could be that Type Ia supernovae do produce a significant amount of magnesium, which keeps the Mg/Fe ratio solar, while O/Fe decreases with increasing metallicity. This would also fit to the slightly higher O/Fe than Mg/Fe ratios in metal-poor stars of the Milky Way (Bensby et al. 2004). In this case, the standard model for Type Ia nucleosynthesis (the so-called 'W7' model; Nomoto, Thielemann, & Yokoi 1984) needs to be revised. This leads to the speculation that the importance of Type Ia enrichment may increase steadily

with atomic number of the element up to Fe and Ni. If this is the case, the higher the atomic number of the element, the flatter should be the X/Fe-Fe/H relation in the Milky Way. In particular elements with high atomic number should have lower X/Fe ratios in the metal-poor halo stars, which has not been confirmed in the review of McWilliam (1997). Maybe new data sets will revolutionize this statement. If true, the low Ca/Mg ratios of early-type galaxies (e.g. Thomas et al. 2003a) would naturally be explained in terms of delayed Type Ia supernova enrichment (Pipino & Matteucci 2004).

The relevant inference for this paper would be that the formation timescales discussed in Section 6 (Eqn. 4) are underestimated. A detailed investigation and quantification of this effect goes far beyond the scope of this paper, and in particular cannot be performed in a straightforward way as the appropriate Type Ia nucleosynthesis calculations are not available. Note however, that the high α/Fe ratios derived here for massive galaxies, suggesting short star formation timescales, are coupled with old average ages, which further reinforces this interpretation. The results of this work suggest star formation timescales as short as only a few 10^8 years in the most massive early-type galaxies with $M_* \sim 10^{12} M_\odot$. It would certainly be desirable if such extreme timescales were slightly relaxed by the additional contribution from Type Ia supernovae to the enrichment of the heavier α -elements. It should be emphasized that a fundamental conclusion of this paper is that low-mass galaxies have more extended formation timescales. This purely differential result is not affected, if Type Ia supernovae represent an additional source of α -elements.

7.2. Comparison to early results

The findings discussed in this paper are supported by a number of evidences from the tightness and the redshift evolution of the scaling relations of early-type galaxies (e.g. Aragón-Salamanca et al. 1993; Bender et al. 1993, 1996; Bower et al. 1992; Kodama et al. 1999; Renzini & Ciotti 1993; Saglia et al. 2000; Ziegler et al. 2001; Ziegler et al. 1999, see review by Peebles 2002). It is known since these early (and some more recent) works that the formation ages of the stellar populations in elliptical galaxies have to be above redshifts $z \gtrsim 2$. New in this paper is the detailed disentanglement of star formation histories as a function of galaxy mass and the distinction between dense and loose environments.

We confirm such high formation redshifts for intermediate-mass and massive ($M_* \gtrsim 10^{10} M_\odot$ or $\sigma \gtrsim 140$ km/s) early-type galaxies in dense environments in good agreement also with the recently discovered relationship between globular cluster color and galaxy luminosity (Strader, Brodie, & Forbes 2004) and the $K-z$ relation of powerful radio galaxies (Rocca-Volmerange et al. 2004).

We find, however, that ellipticals in looser environments form at somewhat lower redshifts between $z \sim 2$ and $z \sim 1$. Low-mass galaxies ($M_* \lesssim 2 \cdot 10^{10} M_\odot$ or $\sigma \lesssim 140$ km/s) in low density regions apparently suffer from significant star formation episodes below redshift $z \sim 1$. This paper further adds the conclusion that the stellar populations of more massive early-type galaxies form earlier and faster. This result confirms early, more qualitative estimates by Bender et al. (1996) based on

the redshift evolution of the Mg- σ relation, who had already noted that the formation redshifts of the most massive early-type galaxies in clusters may be even above $z \gtrsim 4$. Here we find that while the formation epoch is delayed in low-density environments by about 2 Gyr, the timescale is independent of the environmental density and depends only on the galaxy's mass concentration.

7.3. The stellar mass density at $z > 1$

The above evidences provide consistent constraints on the epochs when the stellar populations of early-type galaxies have formed. Our results imply that at redshift around $z \sim 1$, the formation of the total stellar mass in early-type galaxies with $M_* \gtrsim 2 \cdot 10^{10} M_\odot$ or $\sigma \gtrsim 140$ km/s in both high and low density environments is almost completed. Stellar mass growth in early-type galaxies below redshift $z \sim 1$ is restricted to low-mass objects in low density environments. As the latter make up only a small fraction of the total mass of a galaxy population, despite them being numerous, we can infer that stellar mass growth in early-type galaxies is largely completed around redshift $z \sim 1$.

This galaxy type is expected to host between 1/2 and 3/4 of the total stellar mass in the universe (Bell et al. 2003; Renzini 1999). As also massive disks are already present at redshifts between 1 and 2 (Ravindranath et al. 2004; Stockton et al. 2004), this implies that at least 50 per cent of the total stellar mass density must have already been formed by $z \sim 1$. Our results further suggest that a significant increase of the stellar mass density between redshifts 1 and 2 should be present caused mainly by the field galaxy population, while at redshifts around 3 the stellar mass density should be dominated by galaxies in high density environments. Depending on the exact partition between objects in high and low environmental densities, this implies the stellar mass density around redshift 3 to be as low as 10–30 per cent of the local value. Observational estimates of the total stellar mass density as a function of redshift are in overall good agreement with this result. Recent studies are consistent with only mild evolution of the order 20 – 30 per cent up to $z \sim 1$ followed by a significant drop in stellar mass density between redshifts 1 and 2 (Bell et al. 2003; Brinchmann & Ellis 2000; Cohen 2002; Dickinson et al. 2003; Fontana et al. 2004; Fontana et al. 2003; Glazebrook et al. 2004; Rudnick et al. 2003). Our result suggests that the significant mass growth in the early-type galaxy population below $z \sim 1$ observed by Bell et al. (2004) is most likely caused by less massive objects.

7.4. Climbing up the redshift ladder

One fundamental consequence from the results of this paper is the prediction that very massive objects $M_* \gtrsim 10^{11} M_\odot$ with very high star formation rates up to several 1000 M_\odot/yr should be present between redshifts 2 and 5.

Such objects have indeed been recently found. At least part of the SCUBA sources at $2 \leq z \leq 3$ turn out to be massive star forming galaxies with extremely high star formation rates up to several 1000 M_\odot/yr (Genzel et al. 2003; Smail et al. 2002; Tecza et al. 2004). These objects are likely to be the precursors of the most massive ellipticals ($M_* \approx 10^{12} M_\odot$) forming in a violent star formation

episode at high redshift. Ly-break galaxies, instead, exhibit more moderate star formation rates of the order a few 10 M_\odot/yr (Baker et al. 2004; Pettini et al. 2001), and may therefore be the precursors of less massive early-type galaxies in Fig. 10 ($M_* \approx 10^{11} M_\odot$) and/or spiral bulges. Moreover, Pettini et al. (2002) find cB58 (a lensed galaxy at redshift $z = 2.73$, Seitz et al. 1998) to have a significantly α -enhanced *interstellar medium*, which is in good agreement with the α/Fe -enhancement derived in this paper for the *stellar population* of local ellipticals.

A further direct inference from Fig. 10 is that massive old, passively evolved galaxies should exist at intermediate redshifts between 1 and 2. Again, these objects have been found. Medium-deep infrared surveys detect a relatively large number of so-called extremely red objects (EROs) between $z \sim 1$ and 1.5, whose SEDs best fit evolved stellar populations (Caputi et al. 2004; Cimatti et al. 2003, 2004; Daddi et al. 2000; Moustakas et al. 2004; Pozzetti & Mannucci 2000; Saracco et al. 2003, 2004; Väisänen & Johansson 2004). The evolved K -selected EROs mentioned above show evidence for strong clustering (Daddi et al. 2003), hence are likely candidates for being the precursors of the cluster objects shown in the top panel of Fig. 10. In a recent paper, Pierini et al. (2004) show that the colors of some 'evolved' EROs are also consistent with a dusty *post*-starburst population with ages around 0.5 Gyr, which fits to the star formation histories shown in Fig. 10 for the low density environment. It would be interesting to investigate the clustering properties of this subclass of EROs, to verify that they preferably are found in low density environments. Also in agreement with our result is the recent finding in K -selected galaxy surveys that the most luminous objects are best fit by older stellar populations at all redshifts up to $z \sim 1$, which implies the typical M/L ratio (in K) of more massive galaxies to be larger than that of less massive ones (Fontana et al. 2004; Glazebrook et al. 2004).

Finally, deeper redshift surveys are now finding evolved objects even at redshifts around 2 and 3 (Caputi et al. 2005; Chen & Marzke 2004; Franx et al. 2003; McCarthy et al. 2004) and massive star forming objects around redshifts 2 and 5 (de Mello et al. 2004; Lehnert & Bremer 2003; Totani et al. 2001) up to $z \sim 6.5$ (Kurk et al. 2004), again in good agreement with the prediction from the properties of local galaxies made in this paper.

To conclude, it seems the two approaches, archaeology of stellar populations in local galaxies and redshift surveys, are converging to a consistent picture in which massive galaxy formation occurs at fairly high redshifts accompanied by violent star formation.

7.5. Models of galaxy formation

This consistent picture of high formation redshifts of the stellar populations in massive (early-type) galaxies severely challenges the conventional semi-analytic models of galaxy formation (Cole et al. 2000; Hatton et al. 2003; Kauffmann et al. 1993; Menci et al. 2003; Somerville & Primack 1999), and their modification has become unavoidable. As reviewed by Somerville (2004), recent renditions of both semi-analytic models

and hydrodynamical simulations of hierarchical galaxy formation (Nagamine et al. 2004) are consistent with the stellar mass function around $z = 1$ and with the cosmic star formation history (see also Fontana et al. 2004), hence global quantities are well reproduced. However, the models have difficulty producing the old average ages of massive galaxies in the local universe, and accordingly the number density of luminous red galaxies at intermediate redshift as well as the high star formation rates in massive objects at high redshifts (Somerville 2004; Somerville et al. 2004).

At least part of the reason for this shortfall may be connected to the way non-baryonic dark matter and baryonic matter are linked. In current models, star formation is tightly linked to the assembly history of dark matter halos, so that galaxies with longer assembly times also form stars on longer timescales. A possible solution to reconcile extended assembly times with fast star formation histories is a scenario, in which massive objects form their stars early and assemble later (Bower et al. 1998; van Dokkum et al. 1999). This picture gets some theoretical support from the fact that the kinematics of massive early-type galaxies require the origin of mergers between bulge-dominated rather than disk galaxies (Khochfar & Burkert 2003; Naab & Burkert 2003). However, in this case, it would be difficult for early-type galaxies to establish the correlation between metallicity and mass reported here. More fundamental modifications of the models are certainly necessary.

Granato et al. (2001) have presented a promising—even though quite heuristic—approach, in which star formation is enhanced in massive systems because of feedback between star formation and AGN activity (see also Cattaneo & Bernardi 2003 and Kawata & Gibson 2004). This idea is now put on physical grounds in Granato et al. (2004), where the evolution of gas in a dark matter halo is described as a function of gravity, radiative cooling, heating by feedback from supernovae, and—most importantly—heating by feedback from the growing active nucleus.

The assumption of a tight interplay between star formation and nuclear activity gets indeed strong observational support from the fact that besides the α/Fe ratio, also black hole mass correlates with velocity dispersion and galaxy mass (Ferrarese & Merritt 2000; Gebhardt et al. 2000). The resulting ‘anti-hierarchical baryonic collapse’ in the Granato et al. (2004) model leads to higher formation redshifts and shorter formation timescales of the stellar populations in massive halos. In this way both the relationship between α/Fe ratio and galaxy mass (Romano et al. 2002), and the presence of old galaxies at $z \sim 1$ (EROs) and of violently star forming objects at $z \sim 3$ (SCUBA sources) are reproduced.

Granato et al. (2004) consider the evolution of massive halos in the framework of semi-analytic models only above redshifts $z \gtrsim 1$. Hence, a fundamental problem that remains to be solved is the accretion of cold gas onto the central galaxy of a dark matter halo at lower redshift leading to late star formation and the galaxy’s rejuvenation.

An important step to a solution of this latter problem might have been recently made by Binney (2004), who suggests a scenario in which gas cooling is the key pro-

cess. Unlike small systems with shallow potential wells, massive galaxies cannot eject but retain their hot gas, the cooling of which is inhibited by an episodically active galactic nucleus. This ‘atmosphere’ of hot gas builds up a shield around the galaxy preventing cool gas to fall in and to form stars. The inclusion of this effect in semi-analytic models of hierarchical galaxy formation would certainly be the right step toward reconciling our current understanding of galaxy formation with the observational constraints set by the stellar populations properties of massive galaxies.

8. CONCLUSIONS

We study the stellar population properties of 124 early-type galaxies (Beuing et al. 2002; González 1993; Mehlert et al. 2003) with velocity dispersions between 50 and 350 km/s in both high and low density environments. From the absorption line indices $H\beta$, $Mg\ b$, and $\langle \text{Fe} \rangle$ we derive ages, metallicities Z/H , and α/Fe element ratios using our abundance ratio sensitive stellar population models (TMB). The α/Fe ratio is the key to determine the formation timescales of the objects, as it quantifies the relative importance of the chemical enrichment from Type II and the delayed Type Ia supernovae. Together with average ages, we use this information to set constraints on the epochs, when early-type galaxies form the bulk of their stars. To get a handle on the effect of correlated errors, we compare the observed sample with mock galaxy samples with properties as close as possible to the observational data in terms of sample size, velocity dispersion distribution, and measurement errors.

For the bulk of the sample we find that all three stellar population parameters age, total metallicity, and α/Fe ratio correlate with velocity dispersion, hence galaxy mass. We show that these results are robust against recent revisions of the local abundance pattern at high metallicities. To recover the observed scatter we need to assume an intrinsic scatter of about 20 per cent in age, 0.08 dex in $[Z/H]$ and 0.05 dex in $[\alpha/\text{Fe}]$. Both zero-point and slope of the $\alpha/\text{Fe}-\sigma$ relation are independent of the environmental density, while the ages of objects in low density environments appear systematically lower accompanied by slightly higher metallicities.

We identify three classes of ‘outliers’ from these relationships. 1) The low-mass objects with $M_* \lesssim 10^{10} M_\odot$ ($\sigma < 130$ km/s) in our sample show clear evidence for the presence of intermediate-age populations. Their line indices are best reproduced with a 2-component model in which a with a 1.5–2 Gyr population with low α/Fe ratios is added to a base population defined by the above relationships. 2) About 20 per cent of the intermediate-mass objects with $10^{10} \lesssim M_*/M_\odot \lesssim 10^{11}$ ($110 \lesssim \sigma/\text{km/s} \lesssim 230$) must have either a young sub-population or a blue horizontal branch. Compared to the low-mass objects, the case for the intermediate-age population is less convincing because of relatively high α/Fe ratios. 3) Most intriguing is a population of massive ($M_* \gtrsim 10^{11} M_\odot$ or $\sigma \gtrsim 200$ km/s) S0 galaxies, only present in the high density sample, that require a major fraction of their stars (~ 70 per cent) to have formed relatively recently at lookback times of about 2–3 Gyr, corresponding to $z \sim 0.2$. Note that these objects, even though being interesting in themselves, represent only a

minor fraction of the total stellar mass budget in early-type galaxies.

The increase of total metallicity, indicating the completeness of chemical processing, mainly reflects the inability of massive galaxies with deeper potential wells to develop galactic winds. The increase of age and α/Fe ratio with σ shows that more massive galaxies form their stellar populations both earlier and faster. Our results suggest that the well-known Mg- σ relation is mainly driven by metallicity (~ 60 per cent contribution) with almost equal share from α/Fe ratio (~ 23 per cent) and age (~ 17 per cent). The increase of α/Fe with velocity dispersion is responsible for the much weaker correlation of $\langle \text{Fe} \rangle$ with galaxy mass.

With a simple chemical evolution model that takes the delayed enrichment from Type Ia supernovae into account, we translate the ages and α/Fe ratios of the above relationships into star formation histories as a functions of galaxy's velocity dispersions and environmental densities. We show that the higher ages and α/Fe ratios of more massive early-type galaxies imply faster formation timescales at earlier epochs. The lower the mass of a galaxy is, the more it suffers from episodes of late star formation extending to redshifts below $z \sim 1$ for galaxies with $M_* \lesssim 10^{10} M_\odot$. Massive early-type galaxies ($M_* \gtrsim 10^{11} M_\odot$) in high density environments form their stellar populations between redshifts 2 and 5. Galaxies in low density environments appear on average 1–2 Gyr younger than their counterparts in high environmental densities, but obey the same relationship between α/Fe ratio and velocity dispersion. This implies that they form on the same timescales, but the epochs of their formation are delayed to lower redshifts between $z \sim 1$ and $z \sim 2$.

The 'archaeology approach' pursued in this paper and observations of the high-redshift universe are now converging to a consistent picture. The results of this work imply that at least 50 per cent of the total stellar mass density must have already been formed by $z \sim 1$, which is in good agreement with observational estimates of the total stellar mass density as a function of redshift. We conclude that significant mass growth in the early-type galaxy population below $z \sim 1$ must be restricted to less massive objects, and a significant increase of the stellar mass density between redshifts 1 and 2 should be present caused mainly by the field galaxy population. As shown here, the properties of local galaxies predict the presence of massive objects with very high star formation rates of the order $1000 M_\odot \text{yr}^{-1}$ around redshifts 2–5, and the existence of old evolved galaxies at redshifts between 1 and 2, both now confirmed observationally.

Current models of hierarchical galaxy formation are consistent with global properties like the stellar mass function, but remain challenged by the ages of local massive galaxies, the number densities of luminous red objects at intermediate redshift, and the high star formation rates in massive objects at high redshifts. The problem seems tightly linked to the (uncertain) treatment of baryonic matter in dark halos, and likely solutions lie in the inclusion of AGN feedback and refinement of gas heating/cooling processes.

We thank the referee, Robert Proctor, for the careful reading of the manuscript and for his very constructive report.

REFERENCES

- Allende Prieto, C., Barklem, P. S., Lambert, D. L., & Cunha, K. 2004, *A&A*, in press, astro
- Aragón-Salamanca, A., Ellis, R. S., Couch, W. J., & Carter, D. 1993, *MNRAS*, 262, 764
- Arimoto, N., & Yoshii, Y. 1987, *A&A*, 173, 23
- Baker, A. J., Tacconi, L. J., Genzel, R., Lehnert, M. D., & Lutz, D. 2004, *ApJ*, 604, 125
- Baldry, I. K., Glazebrook, K., Brinkmann, J., Ivezić, Ž., Lupton, R. H., Nichol, R. C., & Szalay, A. S. 2004, *ApJ*, 600, 681
- Bell, E., McIntosh, D. H., Katz, N., & Weinberg, M. D. 2003, *ApJS*
- Bell, E. F., et al. 2004, *ApJ*, 608, 752
- Bender, R. 1988, *A&A*, 202, L5
- Bender, R., Burstein, D., & Faber, S. M. 1992, *ApJ*, 399, 462
- Bender, R., Burstein, D., & Faber, S. M. 1993, *ApJ*, 411, 153
- Bender, R., & Paquet, A. 1995, in *Stellar Populations*, ed. P. C. van der Kruit & G. Gilmore, IAU Symposium 164 (Dordrecht: Kluwer Academic Publishers), 259
- Bender, R., Ziegler, B. L., & Bruzual, G. 1996, *ApJ*, 463, L51
- Bensby, T., Feltzing, S., & Lundström, I. 2003, *A&A*, 410, 527
- Bensby, T., Feltzing, S., & Lundström, I. 2004, *A&A*, 415, 155
- Bernardi, M., et al. 1998, *ApJ*, 508, 143
- Bernardi, M., et al. 2003, *AJ*, 125, 1882
- Beuing, J., Bender, R., Mendes de Oliveira, C., Thomas, D., & Maraston, C. 2002, *A&A*, 395, 431
- Binney, J. 2004, *MNRAS*, 347, 1093
- Bower, R., Kodama, T., & Terlevich, A. 1998, *MNRAS*, 299, 1193
- Bower, R. G., Lucey, J. R., & Ellis, R. S. 1992, *MNRAS*, 254, 589
- Brinchmann, J., & Ellis, R. S. 2000, *ApJ*, 536, L77
- Caldwell, N., Rose, J. A., & Concannon, K. D. 2003, *AJ*, 125, 2891
- Caputi, K. I., Dunlop, J. S., McLure, R. J., & D. R. N. 2004, *MNRAS*, 353, 30
- Caputi, K. I., Dunlop, J. S., McLure, R. J., & Roche, N. D. 2005, *MNRAS*, submitted, astro-ph/0408373
- Carollo, C. M., & Danziger, I. J. 1994, *MNRAS*, 270, 523
- Carter, D., et al. 2002, *ApJ*, 567, 772
- Cattaneo, A., & Bernardi, M. 2003, *MNRAS*, 344, 45
- Cenarro, A. J., Gorgas, J., Vazdekis, A., Cardiel, N., & Peletier, R. F. 2003, *mnras*, 339, L12
- Chen, H., & Marzke, R. 2004, *ApJ*, submitted, astro=ph/0405432
- Chiosi, C., & Carraro, G. 2002, *MNRAS*, 335, 335
- Cimatti, A., et al. 2003, *A&A*, 412, L1
- Cimatti, A., et al. 2004, *Nature*, 430, 184
- Cohen, J. G. 2002, *ApJ*, 567, 672
- Cole, S., Lacey, C. G., Baugh, C. M., & Frenk, C. S. 2000, *MNRAS*, 319, 168
- Colless, M., Burstein, D., Davies, R. L., McMahan, R. K., Saglia, R. P., & Wegner, G. 1999, *MNRAS*, 303, 813
- Daddi, E., et al. 2000, *A&A*, 361, 535
- Daddi, E., et al. 2003, *ApJ*, 588, 50
- Davies, R. L., et al. 2001, *ApJ*, 548, L33
- Davies, R. L., Sadler, E. M., & Peletier, R. F. 1993, *MNRAS*, 262, 650
- de Freitas Pacheco, J. A., & Barbuy, B. 1995, *A&A*, 302, 718
- De Lucia, G., et al. 2004, *ApJ*, 610, L77
- de Mello, D. F., Daddi, E., Renzini, A., Cimatti, A., di Serego Alighieri, S., Pozzetti, L., & Zamorani, G. 2004, *ApJ*, 608, L29
- Dickinson, M., Papovich, C., Ferguson, H. C., & Budavári, T. 2003, *ApJ*, 587, 25
- Djorgovski, S., & Davis, M. 1987, *ApJ*, 313, 59
- Dressler, A., Lynden-Bell, D., Burstein, D., Davies, R. L., Faber, S. M., Terlevich, R. J., & Wegner, G. 1987, *ApJ*, 313, 42
- Edmunds, M. G. 1990, *MNRAS*, 246, 678
- Faber, S. M., Friel, E. D., Burstein, D., & Gaskell, D. M. 1985, *ApJS*, 57, 711
- Faber, S. M., & Jackson, R. E. 1976, *ApJ*, 204, 668
- Ferrarese, L., & Merritt, D. 2000, *ApJ*, 539, L9
- Fisher, D., Franx, M., & Illingworth, G. 1995, *ApJ*, 448, 119
- Fontana, A., et al. 2004, *A&A*, 424, 23

- Fontana, A., et al. 2003, *ApJ*, 594, L9
- Franx, M., et al. 2003, *ApJ*, 587, L79
- Franx, M., & Illingworth, G. D. 1988, *ApJ*, 327, 55
- Fuhrmann, K. 1998, *A&A*, 338, 161
- Fusi-Peccii, F., & Renzini, A. 1975, *A&A*, 39, 413
- Fusi-Peccii, F., & Renzini, A. 1976, *A&A*, 46, 447
- Gavazzi, G., Bonfanti, C., Sanvito, G., Boselli, A., & Scodreggio, M. 2002, *ApJ*, 576, 135
- Gebhardt, K., et al. 2000, *ApJ*, 539, L13
- Gebhardt, K., Faber, A. M., Koo, D. C., et al. 2003, *ApJ*, 597, 239
- Genzel, R., Baker, A. J., Tacconi, L. J., Lutz, D., Cox, P., Guilloteau, S., & Omont, A. 2003, *ApJ*, 584, 633
- Glazebrook, K., et al. 2004, *Nature*, 430, 181
- González, J. 1993, Phd thesis, University of California, Santa Cruz
- Gorgas, J., Efstathiou, G., & Aragón Salamaça, A. 1990, *MNRAS*, 245, 217
- Granato, G. L., De Zotti, G., Silva, L., Bressan, A., & Danese, L. 2004, *ApJ*, 600, 580
- Granato, G. L., Silva, L., Monaco, P., Panuzzo, P., Salucci, P., De Zotti, G., & Danese, L. 2001, *MNRAS*, 324, 757
- Greggio, L. 1997, *MNRAS*, 285, 151
- Greggio, L., & Renzini, A. 1983, *A&A*, 118, 217
- Greggio, L., & Renzini, A. 1990, *ApJ*, 364, 35
- Hatton, S., Devriendt, J. E. G., Ninin, S., Bouchet, F. R., Guiderdoni, B., & Vibert, D. 2003, *MNRAS*, 343, 75
- Hau, G. K. T., Carter, D., & Balcells, M. 1999, *MNRAS*, 306, 437
- Jørgensen, I. 1999, *MNRAS*, 306, 607
- Jørgensen, I., Franx, M., & Kjaergaard, P. 1995, *MNRAS*, 276, 1341
- Kawata, D., & Gibson, B. K. 2004, *MNRAS*, submitted, astro-ph/0409068
- Kauffmann, G., & Charlot, S. 1998, *MNRAS*, 294, 705
- Kauffmann, G., White, S. D. M., & Guiderdoni, B. 1993, *MNRAS*, 264, 201
- Kelson, D. D., Illingworth, G. D., van Dokkum, P. G., & Franx, M. 2000, *apj*, 531, 137
- Khochfar, S., & Burkert, A. 2003, *ApJ*, 597, L117
- Kobayashi, C., & Arimoto, N. 1997, *ApJ*, 527, 573
- Kodama, T., & Arimoto, N. 1997, *A&A*, 320, 41
- Kodama, T., Bower, R. G., & Bell, E. F. 1999, *MNRAS*, 306, 561
- Korn, A., Maraston, C., & Thomas, D. 2005, *A&A*, submitted
- Kuntschner, H. 2000, *MNRAS*, 315, 184
- Kuntschner, H., & Davies, R. L. 1998, *MNRAS*, 295, L29
- Kuntschner, H., Lucey, J. R., Smith, R. J., Hudson, M. J., & Davies, R. L. 2001, *MNRAS*, 323, 615
- Kuntschner, H., Smith, R. J., Colless, M., Davies, R. L., Kaldare, R., & Vazdekis, A. 2002, *MNRAS*, 337, 172
- Kurk, J. D., Cimatti, A., di Serego Alighieri, S., Vernet, J., Daddi, E., Ferrara, A., & Ciardi, B. 2004, *A&A*, 422, L13
- Lauberts, A., & Valentijn, E. A. 1989, *The Surface Photometry Catalogue of the ESO-Uppsala Galaxies* (Garching: ESO)
- Lee, H., Yoon, S., & Lee, Y. 2000, *AJ*, 120, 998
- Lehnert, M. D., & Bremer, M. 2003, *ApJ*, 593, 630
- Leitherer, C. 1998, in *The Stellar Initial Mass Function*, ed. G. Gilmore & D. Howell, Vol. 142 (San Francisco, CA: ASP), 61
- Longhetti, M., Bressan, A., Chiosi, C., & Rampazzo, R. 2000, *A&A*, 353, 917
- Maraston, C. 1998, *MNRAS*, 300, 872
- Maraston, C. 2004, in *Multiwavelength mapping of galaxy formation and evolution*, ed. R. Bender & A. Renzini, Venice conference 2003 (Springer), in press, astro-ph/0402269
- Maraston, C. 2005, *MNRAS*, submitted
- Maraston, C., Greggio, L., Renzini, A., Ortolani, S., Saglia, R. P., Puzia, T., & Kissler-Patig, M. 2003, *A&A*, 400, 823
- Maraston, C., Kissler-Patig, M., Brodie, J. P., Barmby, P., & Huchra, J. 2001, *A&A*, 370, 176
- Maraston, C., & Thomas, D. 2000, *ApJ*, 541, 126
- Mateo, M. L. 1998, *ARA&A*, 36, 435
- Matteucci, F. 1994, *A&A*, 288, 57
- Matteucci, F., & Greggio, L. 1986, *A&A*, 154, 279
- McCarthy, P. J., et al. 2004, *ApJ*, Letters in press, astro-ph/0408367
- McWilliam, A. 1997, *ARA&A*, 35, 503
- Mehlert, D., Saglia, R. P., Bender, R., & Wegner, G. 1998, *A&A*, 332, 33
- Mehlert, D., Saglia, R. P., Bender, R., & Wegner, G. 2000, *A&AS*, 141, 449
- Mehlert, D., Thomas, D., Saglia, R. P., Bender, R., & Wegner, G. 2003, *A&A*, 407, 423
- Menci, N., Cavaliere, A., Fontana, A., Giallongo, E., Poli, F., & Vittorini, V. 2003, *ApJ*, astro-ph/0311496
- Merluzzi, P., La Barbera, F., Massarotti, M., Busarello, G., & Capaccioli, M. 2003, *ApJ*, 589, 147
- Moustakas, L. A., et al. 2004, *ApJ*, 600, L131
- Naab, T., & Burkert, A. 2003, *ApJ*, 597, 893
- Nagamine, K., Cen, R., Hernquist, L., Ostriker, J. P., & Sprngel, V. 2004, *ApJ*, in pres, astro-ph/
- Nomoto, K., Thielemann, F.-K., & Yokoi, K. 1984, *ApJ*, 286, 644
- Pagel, B. E. J., & Tautvaisiene, G. 1995, *MNRAS*, 276, 505
- Peebles, P. J. E. 2002, in *ASP Conference Series*, Vol. 283, *A New Era in Cosmology*, ed. N. Metcalfe & T. Shanks (Dordrecht: Kluwer Academic Publishers), 351
- Peletier, R. 1989, Phd thesis, Rijksuniversiteit Groningen
- Pettini, M., Rix, S. A., Steidel, C. C., Adelberger, K. L., Hunt, M. P., & Shapley, A. E. 2002, *ApJ*, 569, 742
- Pettini, M., Shapley, A. E., Steidel, C. C., Cuby, J., Dickinson, M., Moorwood, A. F. M., Adelberger, K. L., & Giavalisco, M. 2001, *ApJ*, 554, 981
- Pierini, D., Maraston, C., Bender, R., & Witt, A. N. 2004, *MNRAS*, 347, 1
- Pipino, A., & Matteucci, F. 2004, *MNRAS*, 347, 968
- Poggianti, B., et al. 2001a, *ApJ*, 562, 689
- Poggianti, B., et al. 2001b, *ApJ*, 563, 118
- Poggianti, B. M., Smail, I., Dressler, A., Couch, W. J., Barger, A. J., Butcher, H., Ellis, R. S., & Oemler, A. J. 1999, *ApJ*, 518, 576
- Pompéia, L., Barbuy, B., & Grenon, M. 2003, *ApJ*, 592, 1173
- Pozzetti, L., & Mannucci, F. 2000, *MNRAS*, 317, L17
- Proctor, R. N., Forbes, D. A., & Beasley, M. A. 2004, *MNRAS*, in press, astro-ph/0409526
- Proctor, R. N., Forbes, D. A., Hau, G. K. T., Beasley, M. A., De Silva, G. M., Contreras, R., & Terlevich, A. I. 2004, *MNRAS*, 349, 1381
- Proctor, R. N., & Sansom, A. E. 2002, *MNRAS*, 333, 517
- Puzia, T., Saglia, R. P., Kissler-Patig, M., Maraston, C., Greggio, L., Renzini, A., & Ortolani, S. 2002, *A&A*, 395, 45
- Ravindranath, S., et al. 2004, *ApJ*, 604, L9
- Reimers, D. 1975, *Mém. Roy. Soc. Liège*, 8, 369
- Renzini, A. 1999, *Ap&SS*, 267, 357
- Renzini, A., & Ciotti, L. 1993, *ApJ*, 416, L49
- Renzini, A., & Voli, M. 1981, *A&A*, 94, 175
- Rocca-Volmerange, B., Le Borgne, D., De Breuck, C., Fioc, M., & Moy, E. 2004, *A&A*, 415, 931
- Romano, D., Silva, L., Matteucci, F., & Danese, L. 2002, *MNRAS*, 334, 444
- Rood, R. T. 1973, *ApJ*, 184, 815
- Rose, J. A. 1984, *AJ*, 89, 1238
- Rose, J. A., Bower, R. G., Caldwell, N., Ellis, R. S., Sharples, R. M., & Teague, P. 1994, *AJ*, 108, 2054
- Rudnick, G., et al. 2003, *ApJ*, 599, 847
- Saglia, R. P., Maraston, C., Greggio, L., Bender, R., & Ziegler, B. 2000, *A&A*, 360, 911
- Saglia, R. P., Maraston, C., Thomas, D., Bender, R., & Colless, M. 2002, *ApJ*, 579, L13
- Sanchez-Blazquez, P., Gorgas, J., Cardiel, N., Cenarro, A. J., & González, J. J. 2003, *ApJ*, 509, L91
- Saracco, P., et al. 2003, *A&A*, 398, 127
- Saracco, P., et al. 2004, *MNRAS*, submitted
- Schiavon, R. P., Rose, J. A., Courteau, S., & MacArthur, L. A. 2004, *ApJ*, 608, L33
- Seitz, S., Saglia, R. P., Bender, R., Hopp, U., Belloni, P., & Ziegler, B. 1998, *MNRAS*, 298, 945
- Smail, I., Ivison, R. J., Blain, A. W., & Kneib, J.-P. 2002, *MNRAS*, 331, 495
- Somerville, R. 2004, in *Multiwavelength mapping of galaxy formation and evolution*, ed. R. Bender & A. Renzini, in press, astro-ph/0401570 (Berlin: Springer)
- Somerville, R. S., et al. 2004, *ApJ*, 600, L135
- Somerville, R. S., & Primack, J. R. 1999, *MNRAS*, 310, 1087
- Spergel, D. N., et al. 2003, *ApJ*, 148, 175
- Stanford, S. A., Eisenhardt, P. R., & Dickinson, M. 1998, *ApJ*, 492, 461
- Stockton, A., Canalizo, G., & Maihara, T. 2004, *ApJ*, 605, 37
- Strader, J., Brodie, J. P., & Forbes, D. A. 2004, *AJ*, 127, 3431
- Surma, P., & Bender, R. 1995, *A&A*, 298, 405

- Tantalo, R., Chiosi, C., & Bressan, A. 1998, *A&A*, 333, 419
 Tecza, M., et al. 2004, *ApJ*, 605, L109
 Terlevich, A., & Forbes, D. 2002, *MNRAS*, 330, 547
 Terlevich, A. I., Kuntschner, H., Bower, R. G., Caldwell, N., & Sharples, R. M. 1999, *MNRAS*, 310, 445
 Thielemann, F.-K., Nomoto, K., & Hashimoto, M. 1996, *ApJ*, 460, 408
 Thomas, D., Greggio, L., & Bender, R. 1998, *MNRAS*, 296, 119
 Thomas, D., Greggio, L., & Bender, R. 1999, *MNRAS*, 302, 537
 Thomas, D., & Maraston, C. 2003, *A&A*, 401, 429
 Thomas, D., Maraston, C., & Bender, R. 2002, *Ap&SS*, 281, 371
 Thomas, D., Maraston, C., & Bender, R. 2003a, *MNRAS*, 343, 279
 Thomas, D., Maraston, C., & Bender, R. 2003b, *MNRAS*, 339, 897
 Thomas, D., Maraston, C., & Korn, A. 2004, *MNRAS*, 351, L19
 Thorén, P., Edvardsson, B., & Gustafsson, B. 2004, *A&A*, in press, astro=ph/0407260
 Totani, T., Yoshii, Y., Iwamuro, F., Maihara, T., & Motohara, K. 2001, *ApJ*, 558, L87
 Trager, S. C., Faber, S. M., Worthey, G., & González, J. J. 2000a, *AJ*, 120, 165
 Trager, S. C., Faber, S. M., Worthey, G., & González, J. J. 2000b, *AJ*, 119, 164
 Treu, T., Stiavelli, M., Casertano, S., Møller, P., & Bertin, G. 2002, *ApJ*, 564, L13
 Tripicco, M. J., & Bell, R. A. 1995, *AJ*, 110, 3035
 Väisänen, P., & Johansson, P. H. 2004, *AJ*, 422, 453
 van den Heuvel, E. P. J. 1975, *ApJ*, 196, L121
 van Dokkum, P. G., Franx, M., Fabricant, D., Illingworth, G. D., & Kelson, D. 2000, *ApJ*, 541, 95
 van Dokkum, P. G., Franx, M., Fabricant, D., Kelson, D. D., & Illingworth, G. D. 1999, *ApJ*, 520, L95
 van Dokkum, P. G., Franx, M., Kelson, D. D., & Illingworth, G. D. 2001, *apjl*, 553, L39
 Vazdekis, A., & Arimoto, N. 1999, *ApJ*, 525, 144
 Vazdekis, A., Kuntschner, H., Davies, R. L., Arimoto, N., Nakamura, O., & Peletier, R. F. 2001, *ApJ*, 551, L127
 Vazdekis, A., Peletier, R. F., Beckmann, J. E., & Casuso, E. 1997, *ApJS*, 111, 203
 Woosley, S. E., & Weaver, T. A. 1995, *ApJS*, 101, 181
 Worthey, G. 1994, *ApJS*, 95, 107
 Worthey, G. 1998, *PASP*, 110, 888
 Worthey, G., & Collobert, M. 2003, *ApJ*, 586, 17
 Worthey, G., Faber, S. M., & González, J. J. 1992, *ApJ*, 398, 69
 Ziegler, B. L., & Bender, R. 1997, *MNRAS*, 291, 527
 Ziegler, B. L., Bower, R. G., Smail, I., Davies, R. L., & Lee, D. 2001, *MNRAS*, 325, 1571
 Ziegler, B. L., Saglia, R. P., Bender, R., Belloni, P., Greggio, L., & Seitz, S. 1999, *A&A*, 346, 13

APPENDIX

DATA SAMPLE

In Table A2 we list list velocity dispersions, line indices $H\beta$, $Mg\,b$, and $\langle Fe \rangle$, galaxy types, environmental densities, literature sources, and classifications of Fig. 4 of the sample investigated. Table A3 gives the stellar population parameters age, metallicity, and α/Fe ratio derived with the TMB models. The $1-\sigma$ errors are estimated through Monte Carlo simulations. We perturb the line indices assuming a Gaussian probability distribution defined by the $1-\sigma$ measurement errors quoted above. The resulting $1-\sigma$ errors correspond to the widths of the distributions in the stellar population parameters from 100 Monte Carlo realization per object.

TABLE A2. SAMPLE PARAMETERS AND LINE INDICES

Name	Sigma	Error	H β	Error	Mg <i>b</i>	Error	\langle Fe \rangle	Error	Type	Environment	Source	Class
NGC 0221	72.1	2.6	2.31	0.05	2.96	0.03	2.75	0.03	E	Low density	Gonzalez	triangles
NGC 0224	156.1	3.7	1.67	0.07	4.85	0.05	3.10	0.04	S0	Low density	Gonzalez	circles
NGC 0315	321.0	3.9	1.74	0.06	4.84	0.05	2.88	0.05	E	Low density	Gonzalez	circles
NGC 0507	262.2	6.4	1.73	0.09	4.52	0.11	2.78	0.10	E	Low density	Gonzalez	circles
NGC 0547	235.6	3.6	1.58	0.07	5.02	0.05	2.82	0.05	E	Low density	Gonzalez	circles
NGC 0584	193.2	2.8	2.08	0.05	4.33	0.04	2.90	0.03	S0	Low density	Gonzalez	squares
NGC 0636	160.3	2.9	1.89	0.04	4.20	0.04	3.03	0.04	E	Low density	Gonzalez	circles
NGC 0720	238.6	5.2	1.77	0.12	5.17	0.11	2.87	0.09	E	Low density	Gonzalez	circles
NGC 0821	188.7	2.9	1.66	0.04	4.53	0.04	2.95	0.04	E	Low density	Gonzalez	circles
NGC 1453	286.5	3.5	1.60	0.06	4.95	0.05	2.98	0.05	E	Low density	Gonzalez	circles
NGC 1600	314.8	4.3	1.55	0.07	5.13	0.06	3.06	0.06	E	Low density	Gonzalez	circles
NGC 1700	227.3	3.0	2.11	0.05	4.15	0.04	3.00	0.04	E	Low density	Gonzalez	squares
NGC 2300	251.8	3.3	1.68	0.06	4.98	0.05	2.97	0.05	E	Low density	Gonzalez	circles
NGC 2778	154.4	3.2	1.77	0.08	4.70	0.06	2.85	0.05	E	Low density	Gonzalez	circles
NGC 3377	107.6	2.6	2.09	0.05	3.99	0.03	2.61	0.03	E	Low density	Gonzalez	squares
NGC 3379	203.2	2.7	1.62	0.05	4.78	0.03	2.86	0.03	E	Low density	Gonzalez	circles
NGC 3608	177.7	3.0	1.69	0.06	4.61	0.04	2.94	0.04	E	Low density	Gonzalez	circles
NGC 3818	173.2	4.2	1.71	0.08	4.88	0.07	2.97	0.06	E	Low density	Gonzalez	circles
NGC 4261	288.3	3.3	1.34	0.06	5.11	0.04	3.01	0.04	E	High density	Gonzalez	circles
NGC 4278	232.5	2.8	1.56	0.05	4.92	0.04	2.68	0.04	E	Low density	Gonzalez	circles
NGC 4374	282.1	2.8	1.51	0.04	4.78	0.03	2.82	0.03	E	High density	Gonzalez	circles
NGC 4472	279.2	4.4	1.62	0.06	4.85	0.06	2.91	0.05	E	High density	Gonzalez	circles
NGC 4478	127.7	4.4	1.84	0.06	4.33	0.06	2.94	0.05	E	High density	Gonzalez	circles
NGC 4489	47.2	3.8	2.39	0.07	3.21	0.06	2.66	0.05	E	High density	Gonzalez	triangles
NGC 4552	251.8	2.8	1.47	0.05	5.15	0.03	2.99	0.03	E	High density	Gonzalez	circles
NGC 4649	309.8	3.0	1.40	0.05	5.33	0.04	3.01	0.03	S0	High density	Gonzalez	circles
NGC 4697	162.4	3.9	1.75	0.07	4.08	0.05	2.77	0.04	E	High density	Gonzalez	circles
NGC 5638	154.2	2.8	1.65	0.04	4.64	0.04	2.84	0.04	E	Low density	Gonzalez	circles
NGC 5812	200.3	3.0	1.70	0.04	4.81	0.04	3.06	0.04	E	Low density	Gonzalez	circles
NGC 5813	204.8	3.2	1.42	0.07	4.65	0.05	2.67	0.05	E	Low density	Gonzalez	circles
NGC 5831	160.5	2.7	2.00	0.05	4.38	0.04	3.05	0.03	E	Low density	Gonzalez	diamonds
NGC 5846	223.5	4.0	1.45	0.07	4.93	0.05	2.86	0.04	S0	Low density	Gonzalez	circles
NGC 6127	238.9	4.4	1.50	0.05	4.96	0.06	2.85	0.05	E	Low density	Gonzalez	circles
NGC 6702	173.8	3.0	2.46	0.06	3.80	0.04	3.00	0.04	E	Low density	Gonzalez	squares
NGC 6703	182.8	2.9	1.88	0.06	4.30	0.04	2.93	0.04	S0	Low density	Gonzalez	circles
NGC 7052	273.8	3.6	1.48	0.07	5.02	0.06	2.84	0.05	E	Low density	Gonzalez	circles
NGC 7454	106.5	2.9	2.15	0.06	3.27	0.05	2.48	0.04	E	Low density	Gonzalez	triangles
NGC 7562	248.0	2.9	1.69	0.05	4.54	0.04	2.87	0.04	E	High density	Gonzalez	circles
NGC 7619	300.3	3.1	1.36	0.04	5.06	0.04	3.06	0.04	E	High density	Gonzalez	circles
NGC 7626	253.1	3.0	1.46	0.05	5.05	0.04	2.83	0.04	E	High density	Gonzalez	circles
NGC 7785	239.6	3.1	1.63	0.06	4.60	0.04	2.91	0.04	E	Low density	Gonzalez	circles
NGC 4874	259.6	4.3	2.13	0.02	4.93	0.02	2.91	0.02	cD	High density	Mehlert	diamonds
NGC 4889	358.7	4.2	1.93	0.03	5.45	0.04	3.04	0.03	cD	High density	Mehlert	diamonds
NGC 4839	275.5	5.8	1.42	0.04	4.92	0.04	2.75	0.04	E	High density	Mehlert	circles
NGC 4841A	263.9	7.5	1.53	0.05	4.51	0.05	2.89	0.04	E	High density	Mehlert	circles
NGC 4926	273.3	4.6	1.50	0.06	5.17	0.06	2.50	0.05	E	High density	Mehlert	circles
IC 4051	258.7	2.1	1.42	0.06	5.34	0.07	2.75	0.05	E	High density	Mehlert	circles
NGC 4895	207.2	1.2	1.68	0.05	4.39	0.06	2.60	0.05	S0	High density	Mehlert	circles
NGC 4860	280.5	4.1	1.39	0.06	5.39	0.07	2.85	0.05	E	High density	Mehlert	circles
NGC 4896	209.1	4.8	1.72	0.06	4.04	0.06	2.67	0.05	S0	High density	Mehlert	circles
NGC 4865	249.7	4.1	2.26	0.08	4.51	0.09	3.01	0.07	S0	High density	Mehlert	diamonds
NGC 4923	186.0	1.9	1.70	0.05	4.43	0.05	2.69	0.04	E	High density	Mehlert	circles
GMP 2413	180.0	3.0	1.80	0.06	4.08	0.06	2.60	0.05	S0	High density	Mehlert	circles
NGC 4840	216.6	2.7	1.63	0.07	4.94	0.07	2.91	0.06	E	High density	Mehlert	circles
NGC 4869	188.1	2.1	1.40	0.05	4.83	0.05	2.90	0.04	E	High density	Mehlert	circles
NGC 4908	192.4	2.7	1.58	0.09	4.58	0.09	2.65	0.07	E	High density	Mehlert	circles
IC 4045	167.3	2.1	1.46	0.06	4.70	0.07	2.77	0.05	E	High density	Mehlert	circles
NGC 4871	154.3	3.0	1.61	0.10	4.36	0.11	2.61	0.09	S0	High density	Mehlert	circles
NGC 4850	155.8	2.0	1.57	0.06	4.39	0.06	2.58	0.05	E	High density	Mehlert	circles
NGC 4883	157.9	2.0	1.58	0.06	4.44	0.06	2.86	0.05	S0	High density	Mehlert	circles
GMP 1853	160.4	5.0	1.63	0.11	4.26	0.12	2.92	0.09	S0	High density	Mehlert	circles
GMP 3661	154.2	4.1	2.25	0.08	4.20	0.08	2.83	0.07	S0	High density	Mehlert	squares
GMP 4679	82.2	2.5	2.39	0.08	3.31	0.09	2.50	0.07	S0	High density	Mehlert	triangles
NGC 4872	171.7	3.1	2.05	0.05	4.05	0.06	2.82	0.04	E	High density	Mehlert	squares
IC 4041	114.2	3.2	2.19	0.08	3.82	0.09	2.82	0.07	S0	High density	Mehlert	squares
NGC 4957	208.4	2.0	1.76	0.03	4.53	0.03	2.93	0.02	E	High density	Mehlert	circles
NGC 4952	252.6	1.7	1.71	0.03	4.76	0.03	2.69	0.02	E	High density	Mehlert	circles
NGC 4944	144.8	1.1	2.13	0.03	3.83	0.03	2.64	0.02	S0	High density	Mehlert	squares
NGC 4931	150.8	1.2	2.10	0.04	3.88	0.05	2.78	0.04	S0	High density	Mehlert	squares
GMP 1990	208.9	2.4	1.40	0.04	4.78	0.04	2.50	0.03	E	High density	Mehlert	circles
NGC 4827	243.7	2.1	1.53	0.03	4.89	0.03	2.80	0.02	E	High density	Mehlert	circles
NGC 4816	231.1	2.4	1.61	0.02	4.87	0.02	2.74	0.02	S0	High density	Mehlert	circles
NGC 4807	178.5	2.0	1.81	0.06	4.39	0.06	2.78	0.05	E	High density	Mehlert	circles

TABLE A2. – CONTINUED.

Name	Sigma	Error	H β	Error	Mg <i>b</i>	Error	(Fe)	Error	Type	Environment	Source	Class
ESO 244G045	185.1	3.7	1.66	0.09	4.12	0.08	2.86	0.05	S0	Low density	Beuing	circles
ESO 1070040	147.0	5.8	2.24	0.25	3.63	0.16	2.97	0.09	E	Low density	Beuing	squares
ESO 1370080	297.3	7.1	1.62	0.18	5.16	0.15	3.18	0.09	S0	High density	Beuing	diamonds
ESO 1480170	134.5	7.5	2.26	0.52	3.49	0.32	2.58	0.20	E	Low density	Beuing	triangles
ESO 1850540	277.2	4.3	1.57	0.06	5.11	0.05	3.07	0.03	E	High density	Beuing	circles
ESO 2210200	153.0	5.0	1.90	0.17	4.01	0.13	2.83	0.08	S0	Low density	Beuing	circles
ESO 3220600	193.2	3.8	1.99	0.17	4.45	0.14	3.08	0.08	S0	High density	Beuing	diamonds
ESO 4230240	182.5	5.5	2.06	0.37	3.84	0.24	2.97	0.14	S0	Low density	Oliveira	squares
ESO 4430240	287.0	7.8	1.75	0.15	5.15	0.13	3.13	0.08	S0	High density	Beuing	diamonds
ESO 4450020	255.5	6.4	1.69	0.09	4.76	0.08	3.02	0.05	S0	Low density	Beuing	circles
ESO 4940350	132.1	2.4	2.20	0.16	3.53	0.12	2.74	0.08	S0	Low density	Oliveira	triangles
IC 1633	347.7	7.9	1.73	0.09	5.42	0.08	2.98	0.05	S0	High density	Beuing	diamonds
IC 3152	167.8	3.7	1.82	0.19	3.66	0.16	2.89	0.10	S0	Low density	Beuing	circles
IC 3986	311.5	7.0	1.87	0.15	5.03	0.12	3.12	0.08	S0	High density	Beuing	diamonds
IC 4797	220.6	6.4	1.92	0.26	4.52	0.18	2.75	0.10	E	Low density	Beuing	circles
IC 4931	289.0	6.0	1.80	0.08	4.76	0.07	3.06	0.04	S0	High density	Beuing	diamonds
IC 5105	308.1	5.4	1.57	0.06	5.26	0.05	2.37	0.03	S0	Low density	Oliveira	circles
NGC 0312	254.8	4.4	1.83	0.09	4.56	0.08	2.48	0.05	E	Low density	Beuing	circles
NGC 0484	244.5	4.5	1.60	0.08	4.41	0.07	2.95	0.04	S0	Low density	Beuing	circles
NGC 0596	161.8	1.6	2.12	0.05	3.95	0.04	2.81	0.03	E	Low density	Oliveira	squares
NGC 0636	178.5	5.0	1.86	0.26	4.38	0.17	2.83	0.09	E	Low density	Oliveira	circles
NGC 0731	162.1	2.6	2.10	0.08	3.92	0.07	2.86	0.04	S0	Low density	Beuing	squares
NGC 1052	202.6	1.7	1.22	0.04	5.53	0.03	2.77	0.02	E	Low density	Beuing	circles
NGC 1172	119.3	1.5	1.82	0.11	3.70	0.08	2.52	0.06	S0	Low density	Oliveira	circles
NGC 1316	223.1	2.1	2.07	0.03	3.90	0.03	2.84	0.02	S0	High density	Oliveira	squares
NGC 1340	175.4	1.5	2.23	0.05	3.99	0.04	3.02	0.03	S0	High density	Oliveira	squares
NGC 1375	75.1	1.5	2.35	0.53	2.68	0.33	2.56	0.20	S0	High density	Beuing	triangles
NGC 1395	250.0	3.0	1.62	0.05	5.21	0.04	2.93	0.03	E	Low density	Oliveira	circles
NGC 1400	256.2	3.0	1.38	0.05	5.16	0.04	2.93	0.03	S0	Low density	Oliveira	circles
NGC 1407	259.7	3.7	1.67	0.07	4.88	0.06	2.85	0.03	E	Low density	Oliveira	circles
NGC 1411	144.0	0.9	1.74	0.04	3.90	0.04	2.57	0.03	S0	Low density	Oliveira	circles
NGC 1549	203.3	1.4	1.79	0.03	4.39	0.03	2.88	0.02	E	Low density	Oliveira	circles
NGC 1553	207.2	1.1	1.88	0.03	4.44	0.03	3.09	0.02	S0	Low density	Oliveira	circles
NGC 2434	180.4	3.9	1.87	0.13	3.72	0.10	2.87	0.07	E	Low density	Beuing	circles
NGC 2717	210.0	6.5	1.91	0.18	4.69	0.14	2.86	0.09	S0	Low density	Oliveira	circles
NGC 2891	100.8	0.6	2.54	0.20	3.07	0.16	2.33	0.11	S0	Low density	Beuing	triangles
NGC 2986	282.2	4.2	1.48	0.06	4.97	0.05	2.92	0.03	E	Low density	Oliveira	circles
NGC 3078	268.1	4.2	1.12	0.09	5.20	0.07	3.16	0.04	E	Low density	Oliveira	circles
NGC 3224	155.8	2.3	2.31	0.14	3.91	0.12	2.92	0.08	E	High density	Beuing	squares
NGC 3923	267.9	3.9	1.87	0.08	5.12	0.07	3.07	0.04	E	Low density	Beuing	diamonds
NGC 4786	291.6	5.8	1.61	0.09	4.57	0.08	2.87	0.05	S0	Low density	Beuing	circles
NGC 5087	303.3	5.1	1.62	0.11	5.39	0.09	3.06	0.05	S0	Low density	Beuing	circles
NGC 5516	313.0	10.1	1.46	0.08	4.81	0.06	3.29	0.04	S0	Low density	Beuing	circles
NGC 5791	271.8	9.8	1.60	0.19	5.06	0.15	3.30	0.10	E	Low density	Beuing	circles
NGC 5903	209.2	3.7	1.68	0.10	4.44	0.08	2.90	0.05	E	Low density	Beuing	circles
NGC 6305	158.9	4.3	2.03	0.13	4.07	0.10	2.80	0.07	S0	Low density	Beuing	squares
NGC 6958	193.9	2.1	1.63	0.05	3.89	0.04	2.75	0.03	S0	Low density	Beuing	circles
NGC 7041	238.7	1.0	1.88	0.03	4.70	0.03	2.52	0.02	S0	Low density	Oliveira	circles
NGC 7185	101.2	1.7	2.35	0.16	3.05	0.13	2.63	0.09	S0	Low density	Beuing	triangles
NGC 7365	115.4	5.5	2.20	0.47	3.25	0.30	2.56	0.18	S0	Low density	Beuing	triangles
NGC 7796	264.1	5.5	1.51	0.08	5.02	0.07	2.78	0.04	S0	Low density	Oliveira	circles

Note. — Cols. 3, 5, 7, 9 give 1- σ errors. Sources for the data (col. 12): González (1993), Beuing et al. (2002), Mehlert et al. (2003), C. Mendes de Oliveira et al. (in preparation). The last column indicates the classification shown by symbol type in Fig. 4.

TABLE A3. RESULTS

Name	Age	Error	[Z/H]	Error	[α /Fe]	Error
NGC 0221	2.4	0.2	0.152	0.030	-0.025	0.013
NGC 0224	7.0	1.7	0.441	0.048	0.219	0.017
NGC 0315	6.6	1.4	0.397	0.038	0.282	0.019
NGC 0507	8.1	1.9	0.261	0.071	0.246	0.040
NGC 0547	10.7	1.7	0.321	0.049	0.311	0.020
NGC 0584	2.8	0.3	0.478	0.046	0.223	0.014
NGC 0636	4.4	0.6	0.376	0.028	0.133	0.013
NGC 0720	5.4	2.4	0.485	0.083	0.353	0.039
NGC 0821	8.9	1.2	0.297	0.036	0.189	0.015
NGC 1453	9.4	1.6	0.380	0.044	0.256	0.018
NGC 1600	9.7	1.9	0.420	0.046	0.263	0.021
NGC 1700	2.6	0.3	0.500	0.049	0.167	0.014
NGC 2300	7.3	1.5	0.427	0.040	0.279	0.017
NGC 2778	6.4	1.9	0.366	0.049	0.268	0.023
NGC 3377	3.6	0.5	0.253	0.035	0.234	0.014
NGC 3379	10.0	1.1	0.299	0.036	0.259	0.012
NGC 3608	8.0	1.5	0.334	0.042	0.213	0.016
NGC 3818	6.7	1.9	0.422	0.053	0.263	0.025
NGC 4261	16.3	1.8	0.275	0.035	0.255	0.015
NGC 4278	12.0	1.3	0.225	0.038	0.331	0.015
NGC 4374	12.8	1.1	0.207	0.032	0.259	0.011
NGC 4472	9.6	1.4	0.342	0.046	0.258	0.021
NGC 4478	5.3	1.2	0.344	0.049	0.180	0.021
NGC 4489	2.0	0.3	0.225	0.043	0.078	0.021
NGC 4552	12.4	1.5	0.356	0.034	0.277	0.011
NGC 4649	14.1	1.5	0.362	0.029	0.296	0.012
NGC 4697	8.3	1.4	0.148	0.043	0.155	0.018
NGC 5638	9.5	0.9	0.274	0.033	0.239	0.015
NGC 5812	6.5	1.0	0.432	0.029	0.226	0.014
NGC 5813	16.6	2.2	0.059	0.042	0.270	0.018
NGC 5831	3.0	0.4	0.504	0.043	0.186	0.017
NGC 5846	14.2	2.2	0.226	0.051	0.270	0.017
NGC 6127	12.6	1.5	0.264	0.044	0.284	0.017
NGC 6702	1.7	0.1	0.686	0.070	0.153	0.017
NGC 6703	4.8	0.8	0.354	0.034	0.180	0.016
NGC 7052	13.2	2.1	0.263	0.050	0.296	0.021
NGC 7454	3.7	0.6	0.032	0.044	0.117	0.021
NGC 7562	8.6	1.3	0.282	0.039	0.219	0.014
NGC 7619	15.4	1.4	0.291	0.031	0.233	0.013
NGC 7626	13.9	1.5	0.251	0.038	0.302	0.013
NGC 7785	9.7	1.6	0.280	0.049	0.209	0.016
NGC 4874	2.4	0.1	0.719	0.026	0.353	0.008
NGC 4889	2.8	0.1	0.769	0.043	0.388	0.020
NGC 4839	15.8	1.4	0.159	0.044	0.300	0.027
NGC 4841A	12.2	1.3	0.178	0.049	0.186	0.024
NGC 4926	14.4	1.7	0.177	0.059	0.428	0.037
IC 4051	15.0	1.9	0.276	0.057	0.374	0.032
NGC 4895	10.4	1.3	0.115	0.054	0.266	0.032
NGC 4860	15.2	2.4	0.315	0.057	0.350	0.038
NGC 4896	9.7	1.4	0.073	0.056	0.170	0.032
NGC 4865	2.0	0.2	0.775	0.114	0.269	0.035
NGC 4923	9.4	1.1	0.180	0.055	0.249	0.037
GMP 2413	8.0	1.5	0.105	0.061	0.214	0.039
NGC 4840	9.2	1.8	0.371	0.058	0.273	0.030
NGC 4869	15.4	1.7	0.190	0.055	0.236	0.034
NGC 4908	12.2	2.5	0.127	0.084	0.278	0.052
IC 4045	14.6	2.1	0.134	0.075	0.255	0.044
NGC 4871	11.9	2.7	0.069	0.103	0.248	0.070
NGC 4850	13.1	1.6	0.037	0.068	0.257	0.055
NGC 4883	11.2	1.9	0.182	0.078	0.184	0.037
GMP 1853	10.2	3.0	0.185	0.112	0.130	0.065
GMP 3661	2.1	0.3	0.543	0.107	0.244	0.040
GMP 4679	2.2	0.3	0.183	0.058	0.150	0.041
NGC 4872	3.5	0.5	0.341	0.064	0.178	0.039
IC 4041	2.5	0.4	0.358	0.070	0.147	0.031
NGC 4957	6.5	0.7	0.351	0.022	0.210	0.011
NGC 4952	8.8	0.8	0.279	0.036	0.316	0.021
NGC 4944	3.3	0.3	0.250	0.033	0.195	0.020
NGC 4931	3.3	0.4	0.306	0.042	0.159	0.023
GMP 1990	18.2	1.6	0.011	0.042	0.349	0.038
NGC 4827	12.0	0.9	0.250	0.041	0.287	0.025
NGC 4816	10.6	0.5	0.267	0.030	0.311	0.020
NGC 4807	6.4	1.5	0.274	0.081	0.232	0.048

TABLE A3. – CONTINUED.

Name	Age	Error	[Z/H]	Error	[α /Fe]	Error
ESO 244G045	9.9	2.1	0.141	0.064	0.121	0.025
ESO 1070040	2.1	2.3	0.414	0.190	0.081	0.059
ESO 1370080	7.0	4.0	0.517	0.130	0.251	0.042
ESO 1480170	2.7	4.0	0.196	0.189	0.153	0.088
ESO 1850540	9.2	1.5	0.434	0.035	0.259	0.014
ESO 2210200	5.1	2.5	0.246	0.112	0.148	0.045
ESO 3220600	3.0	1.7	0.533	0.154	0.192	0.044
ESO 4230240	3.3	4.7	0.324	0.220	0.125	0.083
ESO 4430240	4.4	2.4	0.575	0.107	0.277	0.040
ESO 4450020	7.2	2.0	0.402	0.060	0.223	0.026
ESO 4940350	2.8	1.2	0.226	0.097	0.150	0.043
IC 1633	5.2	1.6	0.563	0.057	0.366	0.024
IC 3152	6.4	3.6	0.132	0.131	0.034	0.051
IC 3986	3.3	2.0	0.623	0.131	0.280	0.039
IC 4797	4.7	4.2	0.362	0.181	0.279	0.067
IC 4931	4.7	1.5	0.475	0.057	0.230	0.023
IC 5105	11.4	1.7	0.210	0.041	0.481	0.013
NGC 0312	7.3	2.0	0.205	0.063	0.362	0.026
NGC 0484	10.4	2.0	0.222	0.059	0.155	0.022
NGC 0596	2.8	0.4	0.360	0.035	0.175	0.015
NGC 0636	4.7	4.1	0.360	0.188	0.225	0.056
NGC 0731	3.1	0.7	0.351	0.066	0.147	0.026
NGC 1052	21.7	1.6	0.222	0.025	0.390	0.007
NGC 1172	7.0	2.3	0.077	0.057	0.088	0.031
NGC 1316	3.2	0.2	0.338	0.023	0.150	0.009
NGC 1340	2.1	0.1	0.490	0.056	0.200	0.014
NGC 1375	2.6	3.1	0.011	0.177	-0.044	0.133
NGC 1395	7.6	1.4	0.439	0.033	0.353	0.013
NGC 1400	15.0	1.6	0.226	0.032	0.338	0.010
NGC 1407	7.4	1.8	0.379	0.044	0.300	0.019
NGC 1411	9.1	0.9	0.042	0.026	0.163	0.015
NGC 1549	6.1	0.6	0.283	0.020	0.237	0.009
NGC 1553	4.7	0.3	0.370	0.017	0.188	0.009
NGC 2434	5.5	2.4	0.167	0.090	0.066	0.038
NGC 2717	3.7	2.8	0.460	0.128	0.300	0.042
NGC 2891	2.0	0.8	0.113	0.099	0.163	0.057
NGC 2986	11.2	1.9	0.347	0.045	0.250	0.014
NGC 3078	22.3	4.2	0.228	0.055	0.250	0.016
NGC 3224	1.9	0.7	0.554	0.139	0.166	0.041
NGC 3923	3.3	0.8	0.623	0.070	0.308	0.022
NGC 4786	10.4	2.4	0.237	0.063	0.213	0.024
NGC 5087	7.3	2.3	0.523	0.068	0.323	0.026
NGC 5516	11.2	2.1	0.380	0.046	0.131	0.017
NGC 5791	6.8	3.9	0.530	0.124	0.199	0.045
NGC 5903	8.8	2.4	0.264	0.075	0.186	0.029
NGC 6305	3.7	1.6	0.322	0.092	0.188	0.035
NGC 6958	11.3	1.0	0.015	0.027	0.097	0.013
NGC 7041	4.6	0.3	0.373	0.025	0.350	0.010
NGC 7185	2.3	0.9	0.145	0.100	0.038	0.047
NGC 7365	3.1	3.4	0.090	0.176	0.095	0.104
NGC 7796	11.8	1.9	0.248	0.050	0.344	0.019

Note. — The stellar population parameters age, total metallicity $[Z/H]$, and $[\alpha/Fe]$ abundance ratio are derived from $H\beta$, $Mg\ b$, and $\langle Fe \rangle$ (Table A2) using SSP models of Thomas et al. (2003b) and Thomas et al. (2004). Cols. 3, 5, 7 give 1- σ errors. The latter are estimated via Monte Carlo simulations (see text).

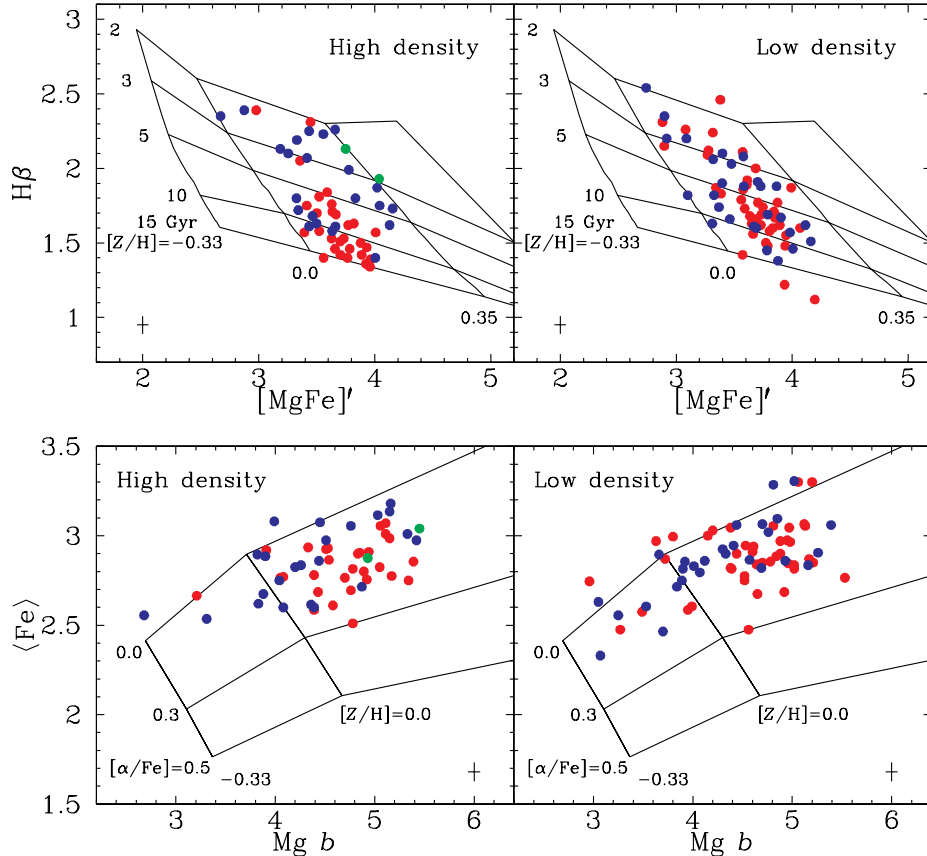


FIG. B11.— Lick indices $[MgFe]'$ versus $H\beta$ (top panels) and $Mg\ b$ versus $\langle Fe \rangle$ (bottom panels). Symbols like in Fig. 2. SSP models with the metallicities $[Z/H] = 0.0, 0.35, 0.67$ are plotted for different ages $t = 2, 3, 5, 10, 15$ Gyr at fixed α/Fe ratio ($[\alpha/Fe] = 0$) (top panels) and different α/Fe ratios $[\alpha/Fe] = 0.0, 0.3, 0.5$ at fixed age ($t = 12$ Gyr) (bottom panels) as indicated by the labels. Different from Fig. 2, the models are corrected for the decrease of O/Fe with increasing metallicity at super-solar metallicity in the solar neighborhood assuming oxygen and the other α -elements being lumped together.

THE LOCAL ABUNDANCE PATTERN AT HIGH METALLICITIES

In a recent study, Proctor et al. (2004) argue that the correlation of α/Fe with velocity dispersion is an 'artefact of incomplete calibration (of the models) to the Lick system'. The basis for their conclusion is the recent finding of Bensby et al. (2004), that the Milky Way disk stars with super-solar metallicities do not have solar but sub-solar O/Fe ratios, O/Fe decreasing with increasing Fe/H (see also Allende Prieto et al. 2004; Pompéia et al. 2003). Stellar population models, being calibrated with these stars, are then likely to reflect sub-solar O/Fe ratios at high metallicities. If the element Oxygen is taken as representative for all α -elements, this would obviously lead to an overestimation of the O/Fe ratio (or α/Fe ratio) in stellar populations with super-solar metallicities like early-type galaxies. Proctor et al. (2004) show that the correction for this effect makes the α/Fe - σ relation disappear.

However, there is a further very important (and somewhat puzzling) point shown in Bensby et al. (2004). All the other α -elements, Mg, Si, Al, Na, Ca, and Ti, do not show this pattern, but level-off at a solar X/Fe ratio in stars with super-solar metallicities (Bensby et al. 2003; Fuhrmann 1998). Only the element oxygen (and maybe also Carbon, Thorén, Edvardsson, & Gustafsson 2004) sticks out of this homogeneous behavior. This differential pattern between Oxygen and the other α -elements cannot be neglected in models taking the local abundance pattern at high metallicities into account. This is particularly important in the context of this work, as the α/Fe ratios presented here are derived from the absorption line indices $Mg\ b$ and $\langle Fe \rangle$, which are sensitive mostly to the elements Fe and Mg, but *not* O (Korn et al. 2005; Tripicco & Bell 1995).

We investigated this issue constructing two additional flavors of stellar population models that account for the local abundance pattern at high metallicity. One in which Oxygen is taken as representative for all α -elements assuming these elements to be enriched in lockstep (like in Proctor et al. 2004), and one in which Oxygen is detached from the rest of the α -elements as discussed above. The decrease of O/Fe with metallicity is adopted directly from Bensby et al. (2004) and can be parameterized as (Proctor et al. 2004):

$$[O/Fe] = -0.5 [Fe/H] \text{ for } [Fe/H] > 0. \quad (B1)$$

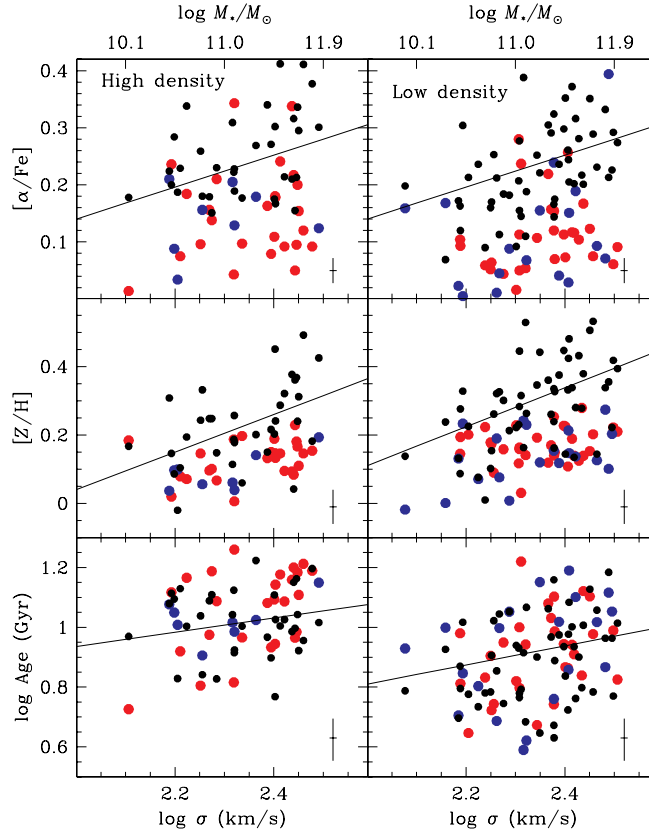


FIG. B12.— Stellar population parameters as a functions of velocity dispersion (measured within $1/10 r_e$) and stellar mass (upper x-axis) for the ‘old’ subpopulation (see Fig. 6). Ages and element abundances are derived with the SSP model of Fig. B11. Black points are Monte Carlo simulations assuming Eqn. 1 (solid lines), which reproduce the data in Fig. 6.

Oxygen and α -elements in lockstep

The resulting model in the index-index planes, assuming oxygen as a representative for all α -elements, is shown in Fig. B11 (equivalent to Fig. 2).

The effect is striking. As oxygen dominates metallicity, the correction for the sub-solar O/Fe of the calibrating stars at high metallicities has the effect that the models are practically ‘labeled’ with lower metallicities. As a consequence, stronger metal indices at a given metallicity are predicted, which leads to the derivation of somewhat lower (but still super-solar) metallicities (top panel of Fig. B11). The derived ages, instead, remain the unchanged. Even more dramatic is the modification of the model in the Mg b -(Fe) plane (bottom panel). At super-solar metallicity, the O/Fe (hence α /Fe in this case) of the original model based on the local abundance pattern has to be increased in order to obtain solar-scaled abundance ratios. This is achieved mainly by decreasing the abundance of iron, so that the iron indices get weaker and the Mg b index get stronger (due to the inverse response to Fe abundance, see TMB for details). The model slope in this diagram is now close to the slope of the data, which clearly impacts on the derived α /Fe- σ relation.

For a better illustration, the stellar population parameters of the galaxy sample investigated here obtained with this model are plotted in Fig. B12 (the equivalent to Fig. 6). The relationships of Eqn. 1 plus the Monte Carlo realizations of Fig. 6 are also shown for comparison. The α /Fe ratios are lower by about 0.1 dex, and in particular the α /Fe- σ relation disappears. Metallicities are also lower by about 0.1 dex, and the Z/H - σ relationship gets significantly tighter. These findings are in agreement with the conclusions of Proctor et al. (2004). Note that the ages do not change.

Oxygen and α -elements separated

In this second flavor of the model we account for the fact that the other α -elements (in particular magnesium) actually do not follow the decrease of the local O/Fe ratio with increasing metallicity at super-solar metallicities (Bensby et al. 2004), hence $[\text{Ne}, \text{Mg}, \text{Si}, \text{S}, \text{Ar}, \text{Ca}, \text{Ti}/\text{Fe}] = 0$ for $[\text{Fe}/\text{H}] \geq 0$. The impact on the index-index diagrams is shown in Fig. B13. The model is almost indistinguishable from the original model used for the analysis of this paper (Fig. 2) and very different from the model in which oxygen and the other α -elements are lumped together (Fig. B11). The reason is the following. Oxygen contributes almost half, and the rest of the α -elements about one quarter to total metallicity. A variation of the α /Fe ratio *including oxygen* is therefore obtained mainly by a modification of Fe abundance (Trager et al. 2000b, and TMB).

The correction from the local sub-solar O/Fe to solar element ratios is therefore achieved by a decrease of Fe

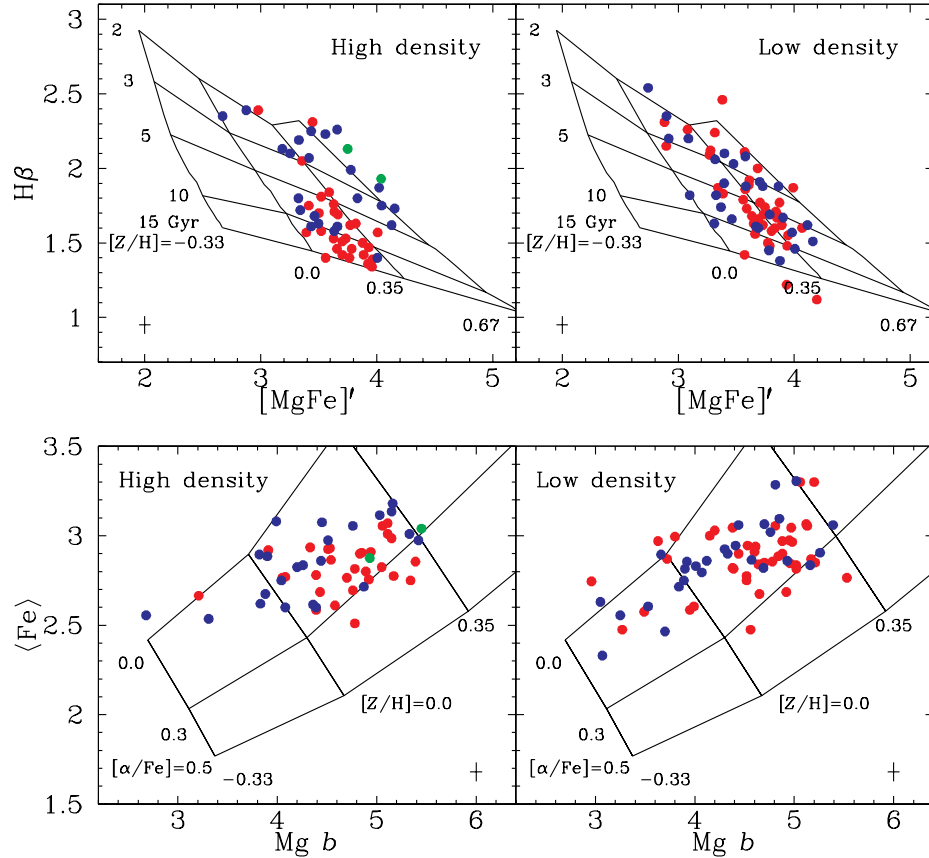


FIG. B13.— Lick indices $[MgFe]'$ versus $H\beta$ (top panels) and $Mg b$ versus $\langle Fe \rangle$ (bottom panels). Symbols like in Fig. 2. SSP models with the metallicities $[Z/H] = 0.0, 0.35, 0.67$ are plotted for different ages $t = 2, 3, 5, 10, 15$ Gyr at fixed α/Fe ratio ($[\alpha/Fe] = 0$) (top panels) and different α/Fe ratios $[\alpha/Fe] = 0.0, 0.3, 0.5$ at fixed age ($t = 12$ Gyr) (bottom panels) as indicated by the labels. Different from Fig. 2, the models are corrected for the decrease of O/Fe with increasing metallicity at super-solar metallicity in the solar neighborhood assuming oxygen and the other α -elements being separated.

abundance by 40 per cent. When oxygen is detached from the other α -elements, instead, the picture is very different. The required decrease of Fe abundance is only 20 per cent, which reduces both the decrease of the Fe indices and the increase of $Mg b$ (note that $Mg b$ responses inversely to Fe abundance). On top of this, the abundances of the other α -elements (including magnesium) need to be reduced by the same amount to maintain the solar α/Fe ratio. This leads to a further decrease of $Mg b$ and an increase of the Fe indices, the latter being inversely coupled with Mg abundance (Korn et al. 2005; Tripicco & Bell 1995). The effect is sufficient to bring the model back to its original position. As a consequence, the stellar population parameters derived with this model are in excellent agreement with the ones presented in this work as shown in Fig. B14.

To conclude, when the non-solar O/Mg ratios of metal-rich stars in the solar neighborhood are taken into account, the correction for the local abundance pattern has no significant impact on the model. This implies that the results of this paper are robust against this problem. In particular, the α/Fe - σ relation found here is real and not caused by calibration artefacts.

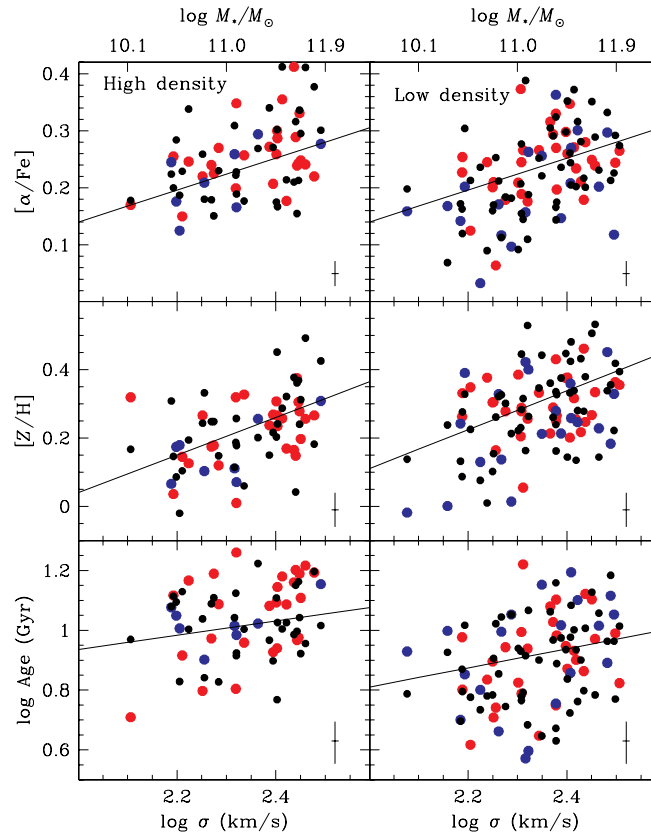


FIG. B14.— Stellar population parameters as a functions of velocity dispersion (measured within $1/10 r_e$) and stellar mass (upper x-axis) for the 'old' subpopulation (see Fig. 6). Ages and element abundances are derived with the SSP model of Fig. B13. Black points are Monte Carlo simulations assuming Eqn. 1 (solid lines), which reproduce the data in Fig. 6.